Optics and biophotonics of nanoparticles with a plasmon resonance

N.G. Khlebtsov

Contents

Abstract. **A brief review of the state of the art in theoretical and experimental studies of the optical properties of metal particles with dipole and multipole plasmon resonances is presented. Metal spheres, nanorods, spherical and elliptic metal nanoshells are considered. The tuning of plasmon resonances of nanoparticles by varying their size, shape, structure, and dielectric environment is described. A large amount of spectrophotometric data on dimensional characteristics of gold colloidal particles is critically analysed and a new calibration of the dependence of their average size on the extinction plasmon resonance wavelength is proposed. A drastic difference between gold and silver colloids in the region of small deviations of their form from spherical is discussed. An example of the excess over not only the Rayleigh limit for the scattering depolarisation factor for dielectric needles (1/3) but also over the plasmon-resonance limit for metal thin rods (3/4) is presented for the first time. The multipole properties of nanorods and universal linear wavelength scaling of multipole resonances are considered depending on the axial ratio of nanoparticles. The outlook for modern trends in biomedical applications of nanoparticles with plasmon resonances is discussed.**

Keywords: *nanoparticles, nanorods, nanoshells, plasmon resonance, absorption and scattering of light, Mie theory, T-matrix method, multipole plasmon resonances, biomedical applications of metal nanoparticles.*

N.G. Khlebtsov Institute of Biochemistry and Physiology of Plants and Microorganisms, Russian Academy of Sciences, prosp. Entuziastov 13, 410049 Saratov, Russia; N.G. Chernyshevsky Saratov State University, ul. Astrakhanskaya 83, 410012 Saratov, Russia;
e-mail: khlebtsov@ibppm.sgu.ru

1. Introduction

Extensive studies of gold and silver nanoparticles with plasmon resonances (PRs) in modern nanobiotechnology [1, 2] resulted in the appearance of a new research field – plasmonics [3]. The use of nanoparticles of noble metals for analytic purposes in biosensorics [4] and genomics [5], for the visualisation of cellular structures [6] (including cancer cells [7, 8]), the targeted delivery of drugs [9], the enhancement of an immune response [10], and the photothermolysis of cancer cells [11 – 14] is based on a combination of the molecular biological 'recognition' (a probe molecule + a

target molecule) and the unique optical properties of these nanoparticles in the visible and IR spectral regions observed upon excitation of localised plasmons [15].

In nanobiotechnology metal nanoparticles are used with recognising biomacromolecules attached to their surface by means of physical adsorption or covalent coupling (for example, single-stranded oligonucleotides, antibodies, etc.). Such nanostructures are called bioconjugates [1] or simply conjugates, while the attachment of biomacromolecules to the nanoparticle surface is often called 'functionalisation' [16]. Thus, a probe conjugate molecule is used for unique coupling with a target, while a metal core is applied for visualisation of the interaction in diagnostics with the help of resonance light scattering in dark-filed microscopy [17], as a contrasting agent in optical coherence tomography (OCT) [18] or for thermal photodestruction of cancer cells due to a rapid heating of nanoparticles by laser pulses [19].

Nanostructures used in biomedicine [1, 2, 20] should have optical resonances within the transparency window of biological tissues [21]. The spectral tuning of PR nanoparticles and the relation between their absorption and scattering coefficients are controlled by the choice of a metal and by varying the size, shape, and structure of nanoparticles [1, 22–25]. Until recently, nearly spherical colloidal gold nanoparticles were used in most applications [10, 26]. The rapid development of the technology of synthesis of nanoparticles for the last $10-15$ years [2, 27, 28] has provided wide possibilities for researchers, beginning from the use of gold nanorods [29–37] and nanoshells [38–41], which are well known now, and ending by exotic structures such as nanorice [42], nanostars [43], nanonecklaces [44], and nanocages [45].

A small size of nanoparticles compared to the wavelength of visible light allows one to use in many cases the dipole approximation developed in classical works of Rayleigh [46] and then generalised by Mie [47] for colloidal spherical gold particles and by Gans [48] for metal rods. We consider the application of this approximation for the description of optical properties of PR nanoparticles, including the universal description of multilayer shells based on the principle of dipole equivalence [49] and comparatively little-known properties such as the depolarisation of scattered light by gold nanorods [50] or silver particles [51]. Because the results of simulation of the optical properties of nanoparticles considerably depend on the permittivity and its size dependence (in particular, due to quantum effects), we discuss this question in more detail than is usually done in physicochemical papers on the optics of metal nanoparticles.

As the size of nanoparticles is increased (the equivolume diameter is ~ 50 nm), their absorption and scattering spectra exhibit a quadrupole resonance [52–54]. In particular, this resonance for nanorods is located, as a rule, between usual short-wavelength and long-wavelength dipole resonances. For submicron nanorods, the structure of the visible spectrum is determined namely by multipole resonances [55–57]. Moreover, the multipole description is necessary in some cases even when the nanostructure size is small compared to the wavelength of light. An example of such unusual collective behaviour is the case of metal bispheres [22, 58, 59], when the dipole approximation for each individual particle of size $10-30$ nm is absolutely accurate, while for contacting or closely spaced spheres the multipole expansion converges very slowly and requires

a very large number (more than 30) multipoles for simulations of spectra. Unlike dipole plasmons, the investigations of multipole resonances began only in the last years, and therefore we believe that it is expedient to discuss this topic in this review.

Except the optics of individual particles, the collective behaviour of the interacting PR particles is of great interest for nanobiotechnology [2, 60]. The analysis of its features includes the study of various structures, beginning from one-dimensional chains [22, 61–65] with unusual optical properties [66], which raised recent polemics in the literature [67–69]. Another example is the optics of two-dimensional arrays [70–74], in particular, clusters of spherical particles on a substrate [75] and two-dimensional planar ensembles formed by usual gold or polymer-coated spheres [22], bispheres [2, 76], nanocavities [77, 78] or nanorods [79, 80]. The unusual properties of monolayers of silver nanoparticles in a polymer film [81] and on a glass substrate [82, 83] have been recently discovered. The collective optical properties of such nanostructures have been explained in detail based on the rigorous solution for interacting particles on a substrate [84] only recently [85]. Let us emphasise once more that the specific features of the collective behaviour of interacting nanoparticles are manifested already in a simplest model of two metal spheres and the nanostructure + molecule system [86, 87].

The optical properties of three-dimensional metal clusters [88–91] are of great interest for nanobiotechnology from different points of view. First, they are closely related to the SPIA (sol-particle-immunoassay) method [92], which is used in different variants for the quantitative assay of proteins (first of all, antibodies) [93–97]), lectins [98], nucleic acids [99], and other biomolecules [10]. Second, the enhanced absorption of light by particle clusters in the near-IR region is an important factor determining the efficiency of phototherapy of cancer cells [14, 100]. Third, three-dimensional clusters have the local structural anisotropy [14, 101–103], and therefore the aggregation of nanoparticles is sometimes accompanied by the unusual transformation of absorption spectra, in particular, by the appearance of a resonance long-wavelength peak [22, 104–109]. Taking into account that the optics of interacting nanoparticles and clusters is a separate and quite broad field, we will not discuss collective effects in this review.

2. Surface plasmon resonances of metal nanospheres. The dipole approximation

The absorption and scattering spectra of metal nanoparticles exhibit resonance UV–VIS bands, which are absent in macroscopic samples. The nature of these bands is related to the collective behaviour of conduction electrons in the light wave field. In the electron gas of metals, as in a plasma, collective plasma oscillations can be excited at frequency ω_p in the visible region [110]. An elementary quantum with energy $\hbar\omega_p$ is called a plasmon [15]. Because plasmons are the result of quantisation of classical plasma oscillations, their properties can be derived from Maxwell's equations [15, 110].

Collective fluctuations of the electron density on the boundary of a usual dielectric with the positive permittivity and a metal with the negative permittivity are called surface plasmons [15]. The excitation of surface plasmons by light is

called a surface plasmon resonance (SPR) for planar structures with travelling waves and a localised surface plasmon resonance (LSPR) for metal nanoparticles [111]. These excitations are related to evanescent surface electromagnetic waves, which are not necessarily localised on the interface. Note that the generally accepted definition of the LSPR of metal nanoparticle is absent in the literature. Thus, for example, these resonances are assigned in [110] to the resonances of normal modes corresponding to the vector harmonics in the multipole description of optical properties of a particle at virtual (complex) frequencies. In [107], SPRs are called 'the surface modes of collective oscillations of an electron plasma appearing in small metal particles'. The word 'localised' is absent in this definition. It was directly pointed out in recent review [25] that 'the clear and general interpretation of SPRs in metal nanoparticles is not available today'.

The elementary classical description of a PR in a small metal sphere is as follows [2, 15, 110]. The electric field of an electromagnetic light wave displaces the cloud of free electrons and produces uncompensated charges near a particle surface and corresponding returning forces. As mentioned above, the optical resonance related to these oscillations is called the LSPR. The term 'surface' is used, first, because the returning force is caused by the polarisation of the particle surface. Second, the radial component of the electric field $E_r^{(n)}$ inside the particle changes as r^{n-1} [110], so that it is stronger localised near the particle surface (for $r = a$) with increasing the mode order ($n \gg 1$).

In the general case, the eigenfrequency of such a 'collective' oscillator does not coincide with the wave frequency and is determined by many factors, including the concentration and effective mass of conductive electrons, the shape, structure, and size of particles, interaction between particles, and the influence of the environment. However, for the elementary description of the optics of PR nanoparticles it is sufficient to use a combination of the usual dipole (Rayleigh) approximation and the Drude theory [110]. In this case, the absorption and scattering of light by a small particle are determined by its electrostatic polarisability α_0, which can be calculated by using the optical permittivity $\varepsilon(\omega)$ [or $\varepsilon(\lambda)$], where ω is the angular frequency and λ is the wavelength of light in vacuum. For a small sphere of volume V and radius a in a homogeneous dielectric medium with the permittivity ε_m, we have

$$\alpha_0 = \frac{3V}{4\pi} \frac{\varepsilon - \varepsilon_m}{\varepsilon + 2\varepsilon_m} = a^3 \frac{\varepsilon - \varepsilon_m}{\varepsilon + 2\varepsilon_m}, \tag{1}$$

and the integrated absorption, scattering, and extinction cross sections are [58, 112]

$$C_{ext} = C_{abs} + C_{sca} = \frac{12\pi k}{a^3} \frac{\varepsilon_m \text{Im}(\varepsilon)}{|\varepsilon - \varepsilon_m|^2} |\alpha|^2$$

$$+ \frac{8\pi}{3} k^4 |\alpha|^2 \simeq 4\pi k \text{Im}(\alpha), \tag{2}$$

where $k = 2\pi \varepsilon_m^{1/2}/\lambda$ is the wave number in the medium. Note that the expressions for cross sections contain not the electrostatic polarisability but the renormalised polarisability [113]

$$\alpha = \frac{\alpha_0}{1 + \varphi(ka)a^{-3}\alpha_0}, \tag{3}$$

where the function $\varphi(ka)$ takes into account the radiative decay [114]:

$$\varphi(ka) = 2 + 2(ika - 1)\exp(ika) \simeq -(ka)^2 - i\frac{2}{3}(ka)^3. \tag{4}$$

For very small particles, Eqn (3) is reduced to the known approximations [88, 115]:

$$\alpha = a^3 \frac{\varepsilon - \varepsilon_m}{\varepsilon + 2\varepsilon_m - i(2/3)(ka)^3(\varepsilon - \varepsilon_m)}. \tag{5}$$

Note that the optical theorem can be satisfied only by using the renormalised polarisability [110]. The appearance of the additional imaginary term in the dominator of Eqn (5) is related to the inverse action of the scattered field on an oscillating dipole, i.e. to the work of radiative forces resulting in the decay of oscillations [114]. Various modifications of the polarisability in the DDA method (see, for example, [116]) were discussed in detail in PhD thesis [117].

Below, we will not distinguish the electrostatic polarisability from the renormalised polarisability. In this approximation, the extinction of a small particle is determined by its absorption $C_{abs} = C_{ext} = 4\pi k \text{Im}(\alpha = \alpha_0)$ and scattering can be neglected. One can see from the expressions presented above that the polarisability and optical cross sections can have a strong resonance under the condition

$$\varepsilon(\omega_{max} \equiv \omega_0) = \varepsilon(\lambda_{max}) = -2\varepsilon_m. \tag{6}$$

The PR frequency can be estimated from the elementary Drude theory [110] for the permittivity of a bulky metal

$$\varepsilon(\omega) = \varepsilon_{ib} - \frac{\omega_p^2}{\omega(\omega + i\gamma_b)}, \tag{7}$$

where ε_{ib} is the contribution of interband electronic transitions; ω_p is the frequency of volume plasma oscillations of free electrons; γ_b is the volume decay constant related to the electron mean free path l_b and the Fermi velocity v_F by the expression $\gamma_b = l_b/v_F$. By combining these relations, we obtain

$$C_{abs} = \pi a^2 \frac{12ka\varepsilon_m}{(2\varepsilon_m + \varepsilon_{ib})^2} \frac{\omega_p^2(\gamma_b/\omega)(\omega + \gamma_b)^2}{(\omega^2 + \gamma_b^2 - \omega_0^2)^2 + \omega_0^4\gamma_b^2/\omega^2}, \tag{8}$$

where the resonance plasmon frequency ω_0 and the corresponding wavelength λ_0 are determined by the equations

$$\omega_{max} \equiv \omega_0 = \omega_p[\varepsilon_{ib} + 2\varepsilon_m]^{-1/2},$$

$$\lambda_{max} \equiv \lambda_0 = \lambda_p[\varepsilon_{ib} + 2\varepsilon_m]^{1/2}. \tag{9}$$

Here, $\lambda_p = 2\pi c/\omega_p$ is the wavelength of volume oscillations of an electron plasma [110]. Expression (8) near the resonance frequency is reduced to the Lorentzian profile obtained in pioneering papers [118] and [119]

$$C_{abs} = \pi a^2 \frac{3ka\varepsilon_m}{(2\varepsilon_m + \varepsilon_{ib})^2} \frac{\omega_p^2(\gamma_b/\omega)}{(\omega - \omega_0)^2 + (\gamma_b/2)^2}. \quad (10)$$

Equation (10) determines the very first ($n = 1$) dipole resonance of a spherical particle. Except this dipole resonance, higher multipoles and corresponding multipole (quadrupole, etc.) resonances can be also excited. For each multipole mode the resonance condition exists, which is similar to (6) and corresponds to the resonance of the quadratic polarisability, etc. [111]. For spherical particles, these conditions correspond to the resonance conditions for the partial Mie coefficients [110] $\omega_n = \omega_p[\varepsilon_{ib} + \varepsilon_m(n + 1)\times n^{-1}]^{-1/2}$, where n is the mode (resonance) number.

To understand the physics of LSPRs, it is important to distinguish two possible scenarios of excitation of higher resonances. The first case corresponds to small but non-spherical particles of irregular or uneven shape, when the distribution of induced surface charges is strongly inhomogeneous and does not correspond to the dipole distribution. This inhomogeneous distribution generates higher multipoles even in the case when the system size is certainly much smaller than the wavelength of light. Prominent examples are cubic particles [25] or two contacting spheres [59]. As mentioned above, the field distribution near a particular contact point is so inhomogeneous that multipole expansions converge very slowly or diverge at all.

The second scenario of excitation of higher multipoles is realised with increasing the particle size, when the transition from the quasi-stationary to radiative regime is observed, and the contribution of higher spherical harmonics should be taken into account in the Mie series (or another multipole expansion). For example, while the extinction spectrum for a spherical silver particle of diameter 30 nm is completely determined by the dipole contribution and has one resonance, the spectrum of a sphere of diameter 60 nm exhibits a distinct high-frequency quadrupole peak in addition to the low-frequency dipole peak. This analysis will be generalised to small nonspherical and multilayer particles in section 4.

3. Optical permittivity of small metal particles

3.1 Size correction of the Drude model

The classical description of the interaction of an electromagnetic wave with atoms of a particle is based on the phenomenological approach with the use of the dielectric function (optical permittivity) $\varepsilon(\omega)$, which enters Maxwell's equations and boundary conditions. The spectral dependence of ε is usually tabulated for massive samples. As the particle size is decreased to the value comparable with the electron mean free path ($a \sim l_e$), deviations of the phenomenological dielectric function $\varepsilon(\omega, a)$ of the particle from the bulky values $\varepsilon(\omega) = \varepsilon(\omega, a \gg l_e)$ can be expected. Of course, the classical description becomes problematic in itself for very small particles (see below). Nevertheless, it seems reasonable to include dimensional effects to the corrected size-dependent dielectric function in the classical description based on the Drude model.

The above-mentioned dipole approximation combined with the Drude model gave a satisfactory agreement between the measured and calculated PR positions for alkali metals (sodium particles in a NaCl crystal), but the experimental resonance width (from 0.05 to 0.6 eV) considerably exceeded the calculated width (0.02 eV). Doyle

[118] assumed that experimental resonance widths correspond to the electron mean free path (3.6 – 1.2 nm) limited by the collisions of electrons with the particle boundary. In other words, the macroscopic electron mean free path in a bulky sample should be replaced by the particle size.

The dielectric functions of colloidal gold particles of average sizes 26 – 30, 13 – 15, and 3 – 4 nm were first measured in [120]. The real and imaginary parts of ε were obtained from spectrophotometric measurements of absorption in a sol and interferometric measurements of its refractive index. The authors of [120] found that the dielectric function for the smallest particles considerably differed from the macroscopic dielectric function and explained this by the limitation of the electron mean free path in accordance with the concept of Doyle.

Beginning from these pioneering studies, the concept of the limited electron mean free path was systematically developed for colloidal silver particles, particles on substrates and embedded into bulk solid matrices [15, 121 – 126], for gold particles deposited on a glass substrate [127], aluminium particles in a KBr matrix [128], and for theoretical simulations of absorption of light in silver shells with a dielectric core [129]. Despite some small differences in treatments, the general recipe for the inclusion of macroscopic tabulated data and size effects to the size-dependent dielectric function consists in the following [15, 122, 127, 130]. Let $\varepsilon_b(\omega)$ be the macroscopic dielectric function, which can be found in the literature from measurements with massive samples [131]. Then, the size-dependent dielectric function of a particle is

$$\varepsilon(\omega, a) = \varepsilon_b(\omega) + \Delta\varepsilon(\omega, a), \quad (11)$$

where the correction $\Delta\varepsilon(\omega, a)$ takes into account the contribution of size-dependent scattering of electrons to the Drude part of the dielectric function described by the expression

$$\Delta\varepsilon(\omega, a) = \varepsilon_b^{Dr}(\omega) - \varepsilon_p^{Dr}(\omega, a)$$

$$= \frac{\omega_p^2}{\omega(\omega + i\gamma_b)} - \frac{\omega_{pa}}{\omega(\omega + i\gamma_p)}. \quad (12)$$

Here, $\gamma_b = \tau_b^{-1}$ is the volume decay constant[*]; τ_b is the electron free path time in a massive metal; ω_{pa} is the plasma frequency for a particle of diameter a (we assume below that $\omega_{pa} \simeq \omega_p$);

$$\gamma_p = \tau_p^{-1} = \gamma_b + \gamma_s = \gamma_b + Av_F/L_{eff} \quad (13)$$

is the size-dependent decay constant equal to the inverse electron mean transit time τ_p^{-1} in a particle; L_{eff} is the effective electron mean free path; γ_s is the size-dependent contribution to the decay constant; and A is a dimensionless parameter determined by the details of scattering of electrons by the particle surface (which is often simply set equal to 1).

The classical value of the effective electron mean path for a sphere is $L_{eff} = a$ (isotropic scattering) or $\frac{4}{3}a$ (diffuse scattering) [132]. According to numerous experimental and

---

[*] The term volume refers here to a parameter measured for massive samples.

theoretical studies [15], the surface scattering constant A depends on a material but not on the particle size. Note here important study [133] where approaches [120] and [134] were developed for determining the dielectric function of silver particles of different sizes by measuring their extinction in the region from 1.5 to 4.5 eV. The author of [133] used the modified Kramers–Kronig relation and determined scattering constants A and 'volume' dielectric functions for gold and silver, which provided accurate fitting for resonance wavelengths and differed from tabulated data [135]. The value $A = 0.7$ found for gold was consistent with estimates obtained by other authors. However, the value $A = 2$ obtained for silver was considerably higher than quantum-mechanical estimates (see below). This discrepancy can be explained by surface effects from adsorbed molecules (see section 3.3).

It is important to note that correction function (12) does not change the contribution $\varepsilon_b(\omega)$ of interband transitions, which seems to be justified because the contribution of d-electrons to the absorption by many metals (for example, gold) is independent of the particle size down to several nanometres. In any case, interband transitions begin contribute to the dielectric function at photon energies $\hbar\omega > \hbar\omega_{ib}$. The separation of contributions from free and bound electrons to the dielectric function of very small gold particles was recently discussed in [136]. Two models for coupled electrons were analysed to obtain the agreement with experimental extinction spectra of very small particles. In the first model, the decay constant of interband transitions and the energy gap were used as fitting parameters, while in the second model the size-dependent density of electronic state was used. It was shown that both models reproduced spectra for particles of size down to 1 nm.

3.2 Size-dependent dielectric function of nonspherical and inhomogeneous particles

Consider now the application of the modified Drude model to nonspherical particles. In [132], the general phenomenological geometrical approach was developed for calculating L_{eff} and the relation

$$L_{eff} = 4V/S \tag{14}$$

was obtained, where V and S are the particle volume and surface area. Equation (14) can be applied to homogeneous particles of any shape. It should be emphasised that (14) determines the isotropic electron mean path even for a certainly anisotropic (nonspherical) particle. For nonspherical particle (for example, ellipsoids), the mean electron transit time can be set equal to

$$\tau_p^{-1} = \sum_{i=1}^{3} \tau_{pi}^{-1} \equiv \gamma_p = \sum_{i=1}^{3} \gamma_{pi}, \quad \gamma_{pi} \equiv \gamma_b + 2v_F/x_i, \tag{15}$$

where x_i is the characteristic diameter of a particle in the direction i. However, as far as we know, approach (15) was never used.

For particles with a dielectric core and a metal shell, the analytic expression [129]

$$L_{eff} = s[2(a/s) - 1]^{1/3} \tag{16}$$

was proposed, which was used to simulate the optical properties of glass containing silver particles with a dielectric core. In Eqn (16), a and s are the shell external radius and thickness, respectively. We used in our paper [138] the expression [137]

$$L_{eff} = a\left[\frac{1}{1+x^2} - \frac{x}{2} - \frac{(1-x)(1-x^2)}{4(1+x^2)} \ln\frac{1-x}{1+x}\right],$$

$$x = \frac{a-s}{a} \tag{17}$$

obtained for the case of isotropic scattering. For thick shells, expressions (16) and (17) give close results ($L_{eff} \sim s$), while for thin shells Eqn (16) gives overestimated values of L_{eff} [138].

Results [132] were applied to inhomogeneous particles of the type of Au/Ag nanorods or Au/Ag [139]. If a particle contains several layers and interfaces, the decay constant is

$$\gamma_p^i = \gamma_b^i + \frac{v_F^i}{L_{eff}^i} = \gamma_b^i + \frac{v_F^i}{4V_i}\sum_j A_{ij}S_{ij}, \tag{18}$$

where v_F^i is the Fermi velocity for the ith metal; S_{ij} is the interface area between metals i and j; and A_{ij} are the corresponding scattering constants. The decay constant for a particle as a whole is found as the mean-weighted values of all the contributions. Although this model is a purely phenomenological formal generalisation of (14) without a reliable substantiation, the authors of [139] showed that it explains a strong broadening of single-particle spectra of Au(core)/Ag(shell) nanorods compared to Ag/Au rods.

3.3 Surface chemical effects

Although many optical properties of small spherical particles can be explained with the help of simple models considered above, there exist considerable discrepancies between the properties of hydrosols (especially, in the case of silver) and sols in other solvents or composites in a solid matrix, which are related to the presence of a double ionic layer at the metal–water interface. Surface physicochemical effects such as cathode and anode polarisation, chemisorption, etc. were discussed in detail in review [140]. These effects can cause the shift of the absorption band of metal colloids, which depends on electrochemical processes at the interface.

As mentioned in section 3.1, the scattering constant for a silver hydrosol considerably differs from its typical value (about 1) for other colloids. It was assumed in theoretical paper [141] that an increase in A can be explained by the influence of the surface layer of adsorbed molecules on the plasmon decay rate. It is accepted at present that the value of A depends on a metal and its local physicochemical environment. Thus, it was shown in [126] that the doping of a SiO_2 matrix with 2-nm silver particles leads to almost threefold increase in the resonance width compared to the case of free particles. This result shows unambiguously that the resonance width is determined by chemical surface effects and can be explained by the Persson model [141] taking into account size and quantum effects. Unfortunately, it is unknown usually which and how many water ions and molecules are adsorbed on the surface of particles prepared by one or another method.

In summary, we can say that the width of the resonance of particles deposited on a substrate or doped into a matrix should be interpreted carefully because a purely dimensional broadening can be weaker than other mechanisms and can be masked by the decay caused by surface chemical effects.

3.4 Quantum-size effects

The unique properties of metal particles are of great interest in connection with an old problem: how many atoms determine the properties of a massive sample?

A typical nanoparticle can be treated as a cluster containing a comparatively small number of atoms, from a few atoms to 10^5. Such clusters occupy the intermediate position between atoms and small molecules, which require a complete quantum-mechanical description, and massive materials described by classical electrodynamics with constitutive equations. Thus, metal particles are mesoscopic objects of size lying between microscopic and macroscopic scales. Because of this, they demonstrate new properties [142], in particular, the discrete spectrum of electronic states and the coherent motion of electrons moving thorough a system without inelastic scattering changing the phases of wave functions. In the language of quantum mechanics, a metal particle located in an external field acquires collective electronic excitations, which are called surface plasmons.

The most important question that should be answered by the quantum-mechanical description concerns the applicability of the modified Drude model (section 3.1). As pointed out in pioneering paper [143], the interpretation of a surface plasmon width in terms of the mean free path is not quite correct due to the appearance of quantum levels, which are determined by the boundary conditions on the surface. By using the theory of a linear response and the fluctuation-dissipative theorem, the authors of [143] obtained the expression

$$\gamma_a = \frac{3}{4}\frac{v_{\mathrm{F}}}{a}\,g\!\left(\frac{\hbar\omega_0}{\varepsilon_{\mathrm{F}}}\right) \tag{19}$$

for the size-dependent contribution to the decay constant [see Eqn (13)], where $g(x)$ is a decaying function of the plasmon energy $\hbar\omega_0$ normalised to the Fermi energy ε_{F}, and $g(0) = 1$. The unexpected result was that *ab initio* analysis gave the same law $\gamma_s \sim 1/L_{\mathrm{eff}} \sim 1/a$ as that based on simple physical [15] and even geometrical [132] considerations. After pioneering paper [143] (which contained many approximations), several refinements were published (see, for example, [141, 144] and references in [15, 133]), but all these studies invariably gave the law $\gamma_s \sim 1/L_{\mathrm{eff}} \sim 1/a$ with small corrections. In fact, all the quantum theories gave the decay law (13), but with different constants A.

From the physical point of view, the size-dependent decay constant (19) is the result of transformation of a surface plasmon to a particle–hole pair via the Landau decay mechanism, which dominates for particles of diameter $1-10$ nm [145]. For large particles, the decay and broadening of plasmon lines are mainly determined by the interaction of plasmons with the electromagnetic field. It follows from Eqn (4) that the contribution of the radiative decay changes proportionally to a particle volume [15]. It is for this reason that the radiative decay can be neglected for particles of diameter smaller than 10 nm, while for particles of diameter smaller than 0.5 nm the interaction of a surface plasmon with an ion lattice can lead to the decay of the collective excitation, whereas the Landau decay is inefficient.

Except surface scattering, there exist other quantum effects [146], which we will not consider in our brief review. Experimental data and theoretical calculations for nanoshells [147, 148] and rods [149] (see also references in [15, 150]) prove the validity of using classical electrodynamics combined with the size-dependent dielectric function. We agree with the opinion of the authors of [110] that the optics of PR particles can be described adequately in terms of classical electrodynamics supplemented by a 'correctly' constructed dielectric function, which can also include, in particular, quantum effects. It is also interesting to note that plasmons in metal nanostructures reveal some analogy with the electronic wave functions of simple atomic and molecular orbitals [151]. It was acknowledged comparatively recently that this analogy and the concept of 'plasmon hybridisation' [152] can be efficiently used for constructing nanostructures and understanding their properties.

3.5 Experiments with individual particles

As long as particles were studied experimentally in solid matrices [15, 110, 153], colloidal solutions [140, 118–121, 128, 130, 133, 138, 154], suspensions of nanoshells (silicon dioxide/gold) [155, 156] or on substrates [15, 126, 127, 129], a certain consensus existed among most of the researchers that the dielectric function should be corrected (as described above) and that such a correction together with the appropriate solution of Maxwell's equations (the Mie theory [47, 110], DDA [115–117, 157] or the T-matrix method [158]) gives a satisfactory agreement between experimental and calculated absorption and scattering spectra.

However, the possibilities of these experiments with ensembles of particles were considerably restricted by an inhomogeneous broadening due to polydispersity and polymorphism of the particles. It was shown recently that the resonance scattering spectra of individual particles can be recorded by using dark-filed microspectrophotometry [17, 159]. This approach completely eliminates the inhomogeneous broadening of an ensemble of particles and allows one to probe 'pure' decay mechanisms [160]. Thus, it was shown in [161] that the width of the scattering resonance of gold nanorods was much smaller than the width of the spectrum of an ensemble of particles and the spectrum of equivolume spheres and was close to the spectral width calculated from permittivities of bulky gold samples. Because excitation of interband transitions in gold requires energy exceeding 1.8 eV, it was predicted that the nonradiative decay in nanorods and nanospheres will be weaker for plasmon energies $E_{\mathrm{res}} < 1.8$ eV. However, the increasing radiative decay in the case of large spheres is considerably stronger than this effect of interband transitions and leads to a greater linewidth. Thus, the high Q factor of the longitudinal resonance of nanorods is explained by a drastic weakening of both interband and radiative decay. An important result of paper [161] was that surface scattering did not contribute considerably to the broadening of the scattering spectrum compared to usual expected estimates [161].

Recently experiments [161] were repeated with rods of sizes varying in a considerably broader range [162] (in addition, the line broadening mechanisms were studied for individual 'nanocells' [163]). It was found that the

linewidth of resonance scattering was determine by the competition between the radiative decay and surface scattering of electrons. Plasmon resonances for thin rods were broadened due to surface scattering, whereas for thick rods the radiative decay dominated. Thus, the measured linewidth consisted of three contributions: the volume contribution Γ_b, the surface scattering of electrons Γ_{surf} [164], and the radiative decay Γ_{rad} [164]:

$$\Gamma = \Gamma_b + \Gamma_{surf} + \Gamma_{rad} \equiv \gamma_b + A \frac{v_F}{L_{eff}} + \hbar\kappa V. \quad (20)$$

Here, the volume contribution can be expressed in terms of the volume dielectric function [15]

$$\Gamma_b = \frac{2\varepsilon_2(\omega_0)}{\left\{ [\varepsilon_1'(\omega_0)]^2 + [\varepsilon_2'(\omega_0)]^2 \right\}^{1/2}} \quad (21)$$

and $\varepsilon_{1,2}'$ denote the derivatives of the real and imaginary parts of the dielectric function of a massive sample. Equation (20) with $A = 0.3$ [165] and $\kappa = 3 \times 10^{-7}$ fs^{-1} nm^{-3} [161, 166] gave reasonable agreement with experimental values (note, however, that the value of A obtained for gold spheres in [133] was 0.7). Although the authors confirmed the presence of the surface scattering mechanism for thin rods, it was assumed that details of the interface structure (i.e. the presence of an adsorption layer) were not important. We suppose that this hypothesis should be verified.

It is pertinent to make here an important remark. It would be erroneous to consider Eqn (20) as the guidance for the modification of the volume dielectric function, i.e. to include all the three mechanisms to the modification of $\varepsilon(\lambda, a)$. It is important to understand that the radiative decay is included into (20) only within the framework of the dipole model. If the optical properties of an individual nanorod are calculated rigorously electrodynamically (for example, by the T-matrix method), the mechanism of radiative decay will be included to the spectrum automatically, so that the dielectric function should be corrected only for surface scattering.

Data [161, 162] for gold nanorods do not answer unambiguously the question about the role of surface scattering. This also concerns gold nanoshells. Indeed, measurements with suspensions [155] showed that surface scattering is the main source of line broadening. However, the width of single-particle spectra [167] was well explained by the Mie theory with volume constants (i.e. not using the dimensional correction). Our experiments [156] showed the presence of two competing broadening mechanisms for nanoshells. In the case of thick gold layers, the main mechanism is related to the inhomogeneous broadening caused by polydispersity. However, in the case of thin shells, the surface scattering of electrons makes the main contribution.

Thus, the data obtained both for nanorods and nanoshells are somewhat contradictory. It seems that this problem requires further experimental studies because the thicknesses of nanoshells in [167] and nanorods in [161] were too large for observation of the limitation of l_b. In addition, single-particle experiments in the region of small sizes (where the most interesting effects should be expected) are strongly complicated due to weak scattering, which is

proportional to the square of the particle volume. For this reason, alternative approaches based on absorption spectra were recently developed [168–171]. In particular, the authors of [172] have managed to record the absorption spectra of individual particles of size down to 5 nm. These experiments revealed unambiguously a considerable contribution of surface electron scattering to the broadening mechanism. Similar experiments were recently performed for gold ellipsoids [173].

Thus, in our opinion, the inclusion of effects of the limitation of the electron mean free path to the Drude model and the use of the classical electrodynamics of individual or interacting particles form a reliable basis for the construction, prediction, and applications of PR nanostructures.

3.6 Tabulated and model dielectric functions

Several data sets for the optical constants of gold films [174, 175] and a single-crystal sample [176] were reported in the literature. The most comprehensive set satisfying the Kramers–Kronig relations was presented in [177]. We used in our papers the so-called second set of constants [177], which was matched with data presented in [178]. At present the most popular data set is based on measurements performed in [135] and included to the handbook [131]. Figure 1 shows the spectral dependences of the real and imaginary parts of the refractive index taken from different sources, together with a spline obtained by analogy with [130]. In particular, spline nodes for wavelengths 210.4–469.9 nm were taken from [175], for 480–640 nm – from [176], and for 657.4–1605 nm – from tables [135]. The most critical is the PR region, and we used data [176] according to recommendations [119] and our own observations [130] showing that constants from [176] give the best agreement between experimental and calculated positions of resonances for carefully measured particle parameters. In our opinion, the data from [175] are most reliable for the short-wavelength range (see Fig. 1), whereas in the region 650–1600 nm we used data from [135].
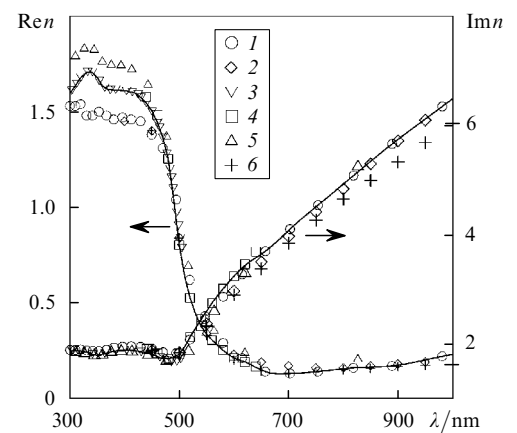

Figure 1. Spectral dependences of the real and imaginary parts of the refractive index of gold [135] (*1*), [174] (*2*), [175] (*3*), [176] (*4*), [177] (*5*), [178] (*6*). The solid curves show spline interpolations (see the text).

According to (12), the correcting addition includes the real and imaginary parts. However, it was found in a number of papers [110, 130, 134, 154] that to obtain the best fit of spectral measurements, it is necessary to correct only the imaginary part, although this recipe, strictly

speaking, is not compatible with the Kramers–Kronig equations. By following [138], we used the expression

$$\varepsilon_2 = \varepsilon_{2b} + \Delta\varepsilon(a) = \varepsilon_{2b} + A \frac{\lambda_p}{L_{eff}} \left(\frac{v_F}{2\pi c} \right) \left(\frac{\lambda}{\lambda_p} \right)^3. \quad (22)$$

In conclusion of this section, we point out an extremely important case when the analytic approximation of the Drude type (12) should be used instead of tabulated data. Such a situation appears, for example, in the finite-difference time-domain method (FDTDM) [179] because the relation between the instant values of the induction and field strength is given by the convolution integral [114]. This convolution could not be calculated at each step in the FDTDM without an analytic solution. This solution can be obtained only by using a few simple models for the spectral dependence of the dielectric function, including the Drude formula. Different authors present different values of parameters in the Drude formula for metal particles. For example, according to [180], the interpolation of data [135] for gold is obtained for $\varepsilon_{ib} = 9.5$, $\omega_p = 8.95$ eV, and $\gamma_b = 0.0691$ eV. For silver, the values of constants in the Drude formula were [180]: $\varepsilon_{ib} = 5.0$, $\omega_p = 9.5$ eV, and $\gamma_b = 0.0987$ eV. According to data [181], the Drude formula approximates measurements [135] for gold for $\varepsilon_{ib} = 12.0$, $\omega_p = 9.49$ eV, and $\gamma_b = 0.0708$ eV. We used in our calculations the values [127] $\omega_p = 8.55$ eV and $\gamma_b = 0.1$ eV.

4. Optical properties of dipole particles with plasmon resonances

4.1 Dependence of resonances of colloidal gold and silver on the particle size

Colloidal gold is known from antique times [27], although the scientific studies of these nanoparticles were pioneered by Faraday [182], Zsigmondy [183], Mie [47], and Svedberg [184]. All aspects of the physical chemistry of colloidal gold were considered in comprehensive review [27]. The history of studies and main results on the optics of colloidal silver were discussed in review [153]. Because the main aspects of the optics of gold and silver colloids were considered in

detail in the literature [110, 140], we do not present here the well-known spectra (with resonances near 520 and 400 nm for gold and silver colloids) and their dependences on the particle size and the refractive index of the environment. Instead, we will discuss only some questions of practical interest or controversial questions.

Let us analyse the dependence of extinction on the particle diameter $d = 2a$. In this paper, the dispersion medium is water with the refractive index $n_m(\lambda)$ calculated by the expression from [130]. The main parameters are the efficiency factor $Q_{ext,sca}$ or optical density A_{ext} and the intensity of scattering at $90°$ at a constant weight concentration c of particles:

$$A_{ext} = 0.651 \frac{cl}{\rho} \frac{Q_{ext}}{d}, \quad (23)$$

$$I_{90}(\lambda) = 0.651 \frac{cl^2}{\rho d} \left[\frac{16 S_{11}(ka, \theta = 90°)}{3(ka)^2} \right], \quad (24)$$

where ρ is the metal density; $Q_{ext} = C_{ext}/\pi a^2$ is the extinction efficiency; $S_{11}(ka, \theta)$ is the normalised intensity of scattering at $90°$ (the first element of the Mueller scattering matrix [110]); and $k = 2\pi n_m/\lambda$ is the wave number in water. The expression in square brackets is normalised so that it is equal to the normalised scattering cross section $Q_{sca} = C_{sca}/\pi a^2$ for Rayleigh particles. Expression (23) was also used to calculate the integrated scattering A_{sca} from Q_{sca}. When it was necessary to compare the efficiencies for individual particles, we used parameters $Q_{ext,sca}$.

Figure 2 presents the dependences of the resonance extinction and scattering intensity on the diameter of silver and gold particles. For a constant weight concentration of a metal, the maximum extinction was achieved for silver and gold particles of diameter ~ 20 and 70 nm, respectively. The maximum specific scattering per unit metal mass was achieved for silver and gold particles of diameter 40 and ~ 100 nm, respectively. Figure 2b presents the relation between integrated scattering and total extinction. Small particles mainly absorb light, whereas large particles mainly scatter it [185]. The contributions of integrated scattering
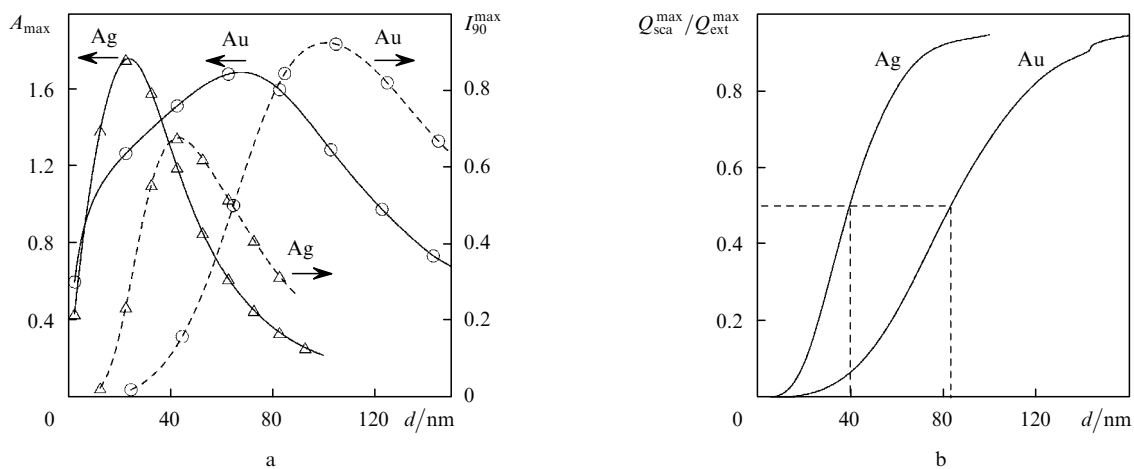

Figure 2. Dependences of the optical density of suspensions and the intensity of scattering at $90°$ on the particle diameter at constant weight concentrations of gold (57 μg mL^{-1}) and silver (5 μg mL^{-1}) (a) and dependences of the integrated scattering and extinction cross sections on the particle diameter at the extinction resonance wavelength (b).

and absorption to extinction become equal when the diameters of silver and gold particles are equal to 40 and 80 nm, respectively.

Although the most reliable measurements of particle sizes are provided by transmission electron microscopy (TEM), it is convenient to have in practice a simple and convenient method for rapid control of particle sizes. In our opinion, usual absorption spectroscopy is such a method. Figure 3a illustrates the principle of measurements by the dependence of the resonance extinction and scattering wavelengths on the diameter of gold and silver particles. The size dependence of the resonance wavelength is determined by the size dependence of the optical constants of nanoparticles in the region of small sizes and by the contribution of higher multipoles with the dominating scattering for particles of diameter exceeding 40 nm. In particular, a drastic change in the size dependence in the region $d \leqslant 10$ nm for extinction resonances of gold (see insert in Fig. 3a) confirmed in experiments [130] is related to the size dependence of optical constants. The wavelengths of extinction and scattering resonances for silver virtually coincide, whereas scattering resonances for gold are shifted to the red with respect to extinction resonances, as follows both from calculations (Fig. 3a) and experiments [186–188].

Based on the dependences of the type presented in Fig. 3a, we proposed [130] the calibration curve for determining the size of spherical gold particles of diameters 5–50 nm obtained by the citrate Frens method [189]. The reliability of this calibration was confirmed by other authors in independent experiments [190, 191]. Figure 3b presents a new calibration curve based on our experimental data [37, 130] and experimental data obtained by other authors [192–199] in the range of particle diameters from 3.5 to 100 nm. The new calibration is described by the equation

$$d = \begin{cases} 3 + 7.5 \times 10^{-5} X^4, & X < 23, \\ [(X - 17)^{1/2} - 1]/0.06, & X \geqslant 23, \end{cases} \quad X = \lambda_{max} - 500, \quad (25)$$

where all the quantities are measured in nanometres. Expression (25) can be used in a much broader range (up to 120 nm) than the previous calibration [130]. Note

that the shape of particles of diameter above 40 nm obtained by the citrate Frens method usually noticeably differs from spherical. Therefore, empirical calibration (25) takes into account to a certain degree the shape effect.

Does calibration (25) correspond to the results of the Mie theory? This question was thoroughly studied in [130], where its was shown that to obtain agreement between measurements and calculations in the range of diameters above 15 nm, it is necessary to take into account the size distribution of particles and the distribution of particles over shape factors. The latter effect was first taken into account in [130] based on the rigorous T-matrix method. In the region of small particle sizes there exists an anomaly – a drastic decrease in the slope of the calibration curve, which is explained, as shown in Fig. 3a (see also [130]) by the size dependence of the dielectric function of gold particles.

The authors of papers [198, 199] published in 2007 reported that the results of their measurements were consistent with calculations performed by using the Mie theory. Figure 4a presents the size dependences of the extinction resonance wavelength calculated according to calibration (25) and the Mie theory taking into account all multipoles. It follows from Fig. 4a, first, that experimental data [198, 199] well agree with our calibration (25) but are inconsistent, unlike the statement of the authors of [198, 199], with our calculations by the Mie theory. One can see that experimental resonance wavelengths from [198, 199] exceed the wavelengths predicted by the Mie theory. Note that the authors of [198] calculated spectra by using the expression from [200] for absorption in the dipole approximation, while the authors of [199] used in calculation the complete Mie theory. It is known from theory [110] and measurements of elastic scattering spectra that the consideration of scattering contribution and higher multipoles to extinction shifts the resonance to the red. For particles of diameter above 40 nm, the use of the dipole approximation in calculations should give the understated values of resonance wavelengths, i.e. the discrepancy between calculations and measurements should be even greater. Therefore, the agreement between calculations and measurements in [198] can be only explained by the difference of
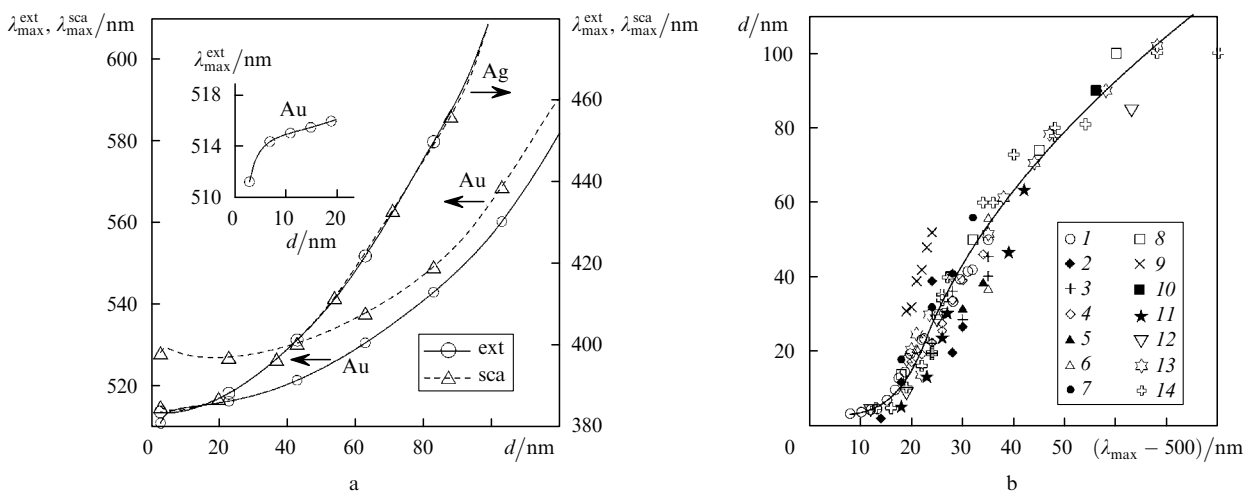

Figure 3. Dependences of the resonance extinction (λ_{max}^{ext}, solid curves) and scattering (λ_{max}^{sca}, dashed curves) wavelengths on the diameter of gold and silver particles (a); the calibration curve for measuring the mean diameter of spherical colloidal particles from the PR extinction wavelength (b): symbols denote experimental data taken from [130] (1), [192] (2–5), [193] (6, 7), [194] (8), [195] (9), [37] (10), [196] (11), [197] (12), [198] (13), and [199] (14); references according to (2–7) see in [192, 193].
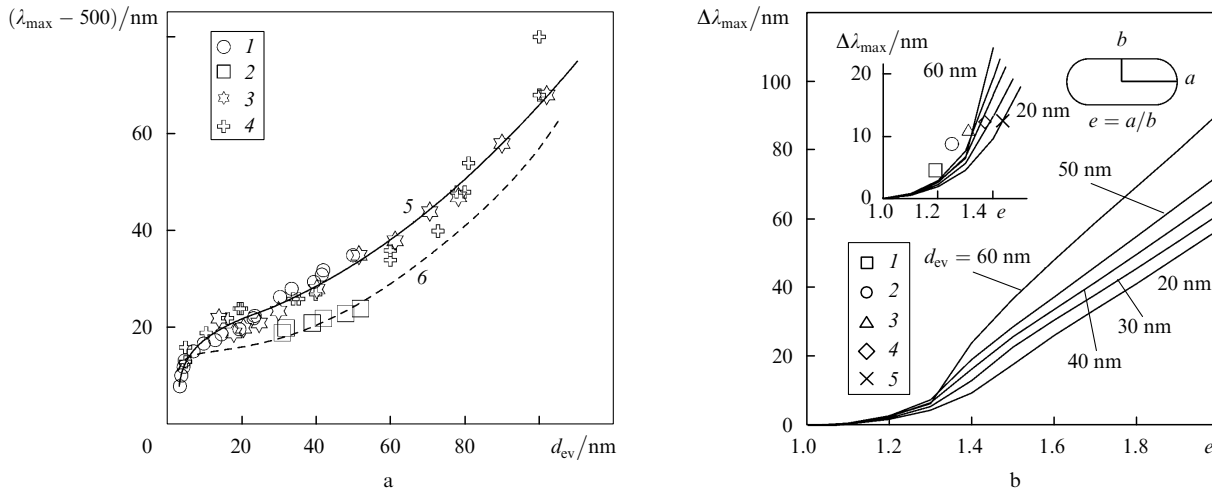
Figure 4. Dependences of the extinction resonance wavelength on the particle diameter according to measurements [130] (*1*), [195] (*2*), [198] (*3*), [199] (*4*), Eqn (25) (*5*), and the Mie theory (*6*) (a) and the dependences of the shift $\Delta\lambda_{max} = \lambda_{max}^{exp} - \lambda_{max}^{Mie}$ of the resonance wavelength for s-cylinders with respect to the resonance of spheres calculated by the T-matrix method for particles with the equivolume diameter $d_{ev} = 20 - 60$ nm; the insert shows the enlarged part of the initial region and points obtained by the approximation of experimental data [192] for particles with $d_{ev} = 20$ (*1*), 30 (*2*), 40 (*3*), 50 (*4*), and 60 nm (*5*) (b).

optical constants used in [198] from ours. This can also explain the discrepancy between data [199] and our calculations by the Mie theory. Another explanation can be the difference of the dielectric function that we used in calculations. However, our spline was carefully verified in [130]. Second, and it is most important, we see that data [195], which strongly differ from other experimental results (Fig. 3b) and do not correspond to calibration (25), well agree with our calculation by the Mie theory. Thus, we assume that all is determined by the shape of particles. It seems that the authors of paper [195] have managed to prepare perfectly spherical monodisperse particles, which they pointed out themselves. It is for this reason that our Mie calculations well agree with their measurements. In all other cases, it is necessary to take into account the deviation of the particle shape from spherical. For example, Fig. 4b shows the red shift of the resonance of weakly nonspherical particles (s-cylinders [37], calculation by the T-matrix method compared to the Mie calculation) depending on their equivolume diameter. The insert shows the enlarged part of the origin of curves together with points obtained by the approximation of experimental data (Table 1 and Fig. 1 from [192])

$$e = \frac{1}{60} d + 1.06, \qquad (26)$$

which were combined with calibration (25). Although we have not obtained very good agreement between calculations and measurements, the data presented in Fig. 4b prove unambiguously that the overstated values of resonance wavelengths are related to the particle shape. In our opinion, it is for this reason that empirical calibration (25) and the averaged set of experimental data (Fig. 3b) are inconsistent with the Mie calculation. In fact, we have made the same conclusion in [130].

In the region of small particle sizes, the data of [198] are inconsistent with our measurements and calculations [130]. However, we are sure that our data are reliable because experimental data presented in [199] are in good agreement with our first measurements [130] and prove unambiguously

the presence of the anomaly in the size dependence of the PR shift discovered for the first time in [130]. Note that spectrophotometric control of the size of gold particles of diameter smaller than 5 nm has specific features [130]. This region was carefully studied in papers [136, 154], where it was shown that even in this case absorption spectra can be used as a reliable and convenient tool for determining particle sizes averaged over the ensemble.

A new method for studying biospecific interactions involving conjugates of colloidal gold nanoparticles was developed in [186 – 188]. The method is based on the measurements of differential static scattering spectra at 90° with the automatic correction of spectral absorption. We have shown that the size dependence of the maxima λ_{max}^{sca} of differential scattering can be used for morphometric analysis of gold sols and have pointed out considerable differences between the experimental dependence $\lambda_{max}^{sca}(d)$ and Mie calculations. As follows from the above discussion, these discrepancies are explained first of all by the difference of the particle shape from spherical. Another important question is related to the inhomogeneous broadening of spectra caused by the dispersion of the particle size. This effect can be used as a simple optical test for the dispersion or partial aggregation. The question is which of the spectra, extinction or scattering, is preferable for this purpose. Numerical simulations and experimental studies have shown [187, 188] that the differential scattering method has in this respect indisputable advantages over spectrophotometry.

This conclusion is illustrated in Fig. 5a which shows the extinction and scattering spectra of gold particles of diameter 25 nm and a mixture of three fractions with the same number of particles of diameters 20, 25, and 30 nm [187]. One can see that the sensitivity of the scattering spectrum to the dispersion composition of the mixture is much higher than that of the extinction spectrum. Theoretical simulation (Fig. 5b) agrees in principle with this result, although the calculated spectra are considerably narrower than experimental ones because the model neglected the polydispersity of fractions themselves and, as we will show below, due to the particle shape effects.
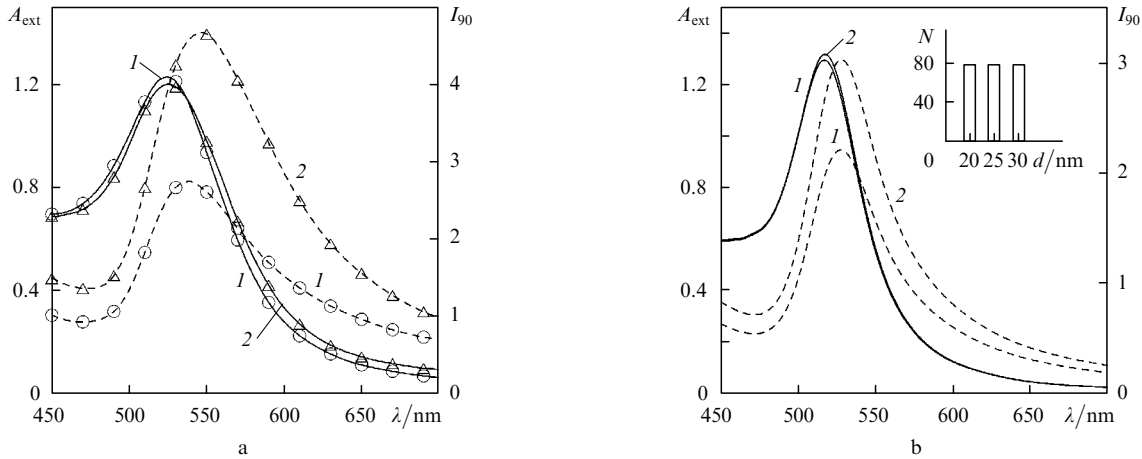
Figure 5. Experimental (a) and theoretical (b) extinction (solid curves) and differential scattering (dashed curves) spectra: (*1*) the initial colloidal gold sol with the diameter of particles 25 nm; (*2*) a mixture with the same amount of particles of diameters 20, 25, and 30 nm (histogram in the insert).

4.2 Gold and silver nanorods

The optical properties of small nanorods were investigated in detail in the dipole approximation by the methods of discrete dipoles and T-matrix [12, 23 – 25, 52, 53, 201 – 208]. At present gold nanorods are prepared, as a rule, by reducing gold on seeds in the presence of cetyltrimethy-lamonium bromide and silver ions [32, 33, 37]. Figure 6 presents the TEM photograph of an NR-655 sample (specific synthesis for obtaining a PR at ~ 650 nm). The main part of particles can be described the geometric model of a cylinder with hemispherical ends (the s-cylinder model [52, 203]). This model was mainly used in our papers. The influence of details of the rod shape was studied in [23, 52, 206 – 208].
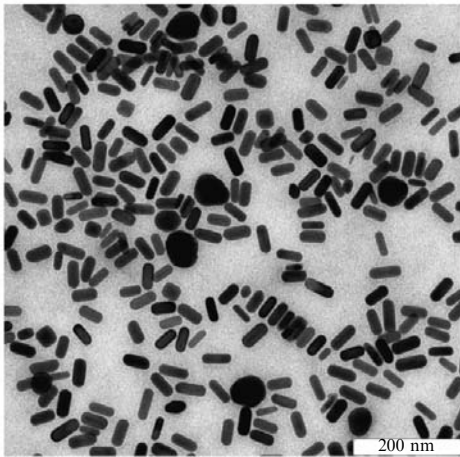

Figure 6. Electron microscope image of an NR-655 sample before the separation of particles. The particles are mainly cylinders with hemispherical ends. A small amount of large particles of irregular shape, bipyramids and cubes are also present.

Along with the s-cylinder model, a convenient approximation for qualitative analysis is an ellipsoid with the known analytic solution for the axial polarisability tensor [46, 48, 110]

$$\alpha_{\parallel,\perp} \equiv \alpha_{a,b} = \frac{V}{4\pi} \frac{\varepsilon - \varepsilon_m}{\varepsilon + (\varepsilon - \varepsilon_m)L_{\parallel,\perp}}, \qquad (27)$$

where the geometrical depolarisation factors [110] satisfy the relation $L_\parallel + 2L_\perp = 1$, and $L = 1/3$ for spheres. Unlike spherical particles, expressions of type (10) now predict the appearance of two resonances corresponding to oscillations of electrons across and along the symmetry axis of a particle. In particular, the supersensitive tuning of the longitudinal resonance is explained by the modification of expression (9)

$$\lambda_\parallel^{max} = \lambda_p[\varepsilon_{ib} + (1/L_\parallel - 1)\varepsilon_m]^{1/2}, \qquad (28)$$

which predicts the strong red shift of the resonance with increasing the axial ratio of particles (when $L_\parallel \to 0$, see below).

Figure 7 shows the extinction and integrated scattering spectra of randomly oriented gold (Figs 7a, c) and silver (Figs 7b, d) nanorods with the equivolume diameter $D = d_{ev} = 20$ nm and the shape factor $1 - 6$. The single-particle extinction and scattering are compared by using the efficiency factors. We see again that the properties of particles depend very strongly on the metal nature. First, as the shape factor for gold is increased, the resonance extinction increases approximately by a factor of five and the Q factor also increases. For silver, vice versa, the highest Q factor is observed for spheres, and the resonance extinction for rods is lower. Second, for the same volume and axial ratio, the extinction and scattering of light by silver rods are considerably more efficient. The resonance scattering factors for silver particles are approximately five times larger than those for gold particles. Third, the relative intensity of the transverse PR of silver particles with the shape factor above 2 is noticeably larger than that for gold particles, where this resonance can be simply neglected. Finally, principal differences are revealed for particles with the shape factor smaller than 2 (Figs 7c, d). The resonance for gold particles shifts to the red and gradually splits into two bands with dominating absorption in the red region. The scattering band shifts to the red and its intensity increases. For silver rods, the situation is different. The short-wavelength resonance shifts to the blue, its intensity
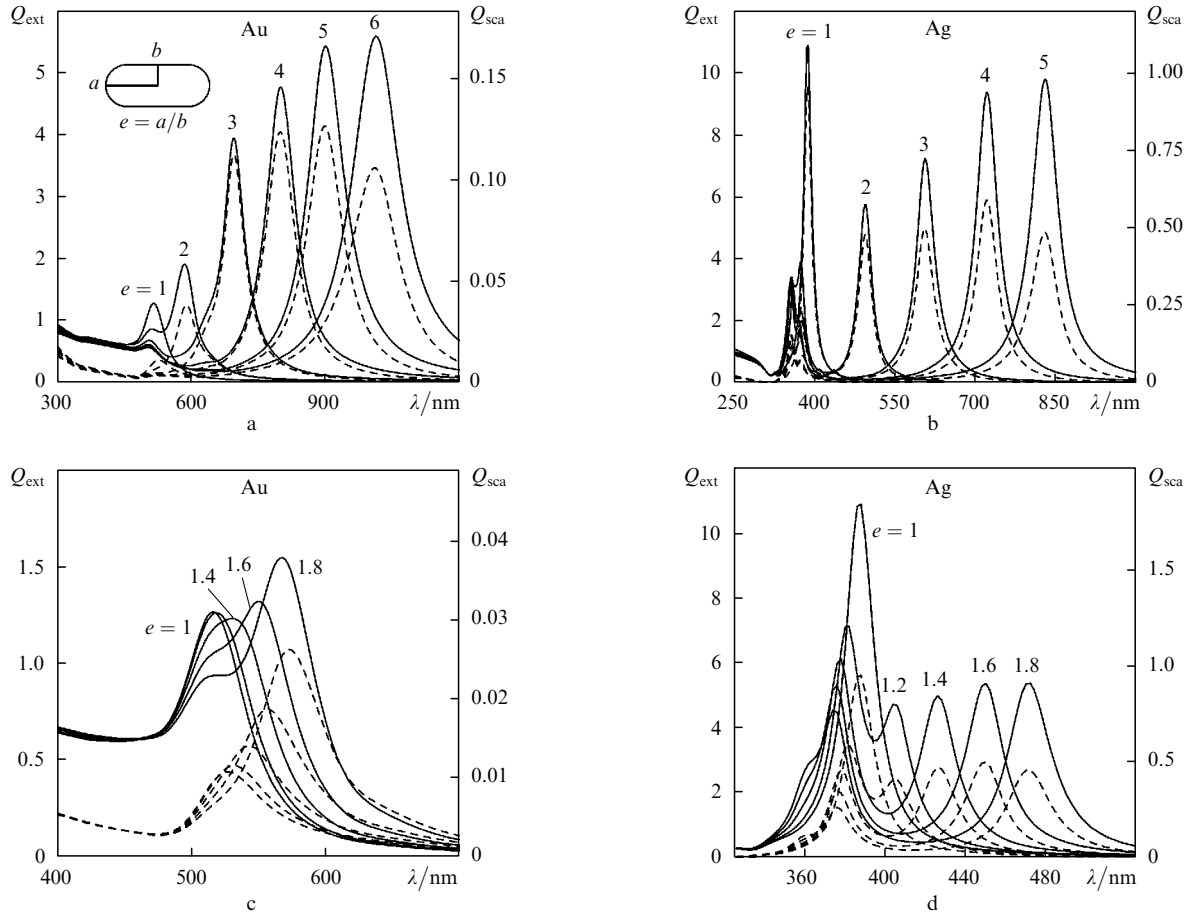
Figure 7. Extinction (solid curves) and scattering (dashed curves) spectra of randomly oriented gold (a, c) and silver (b, d) s-cylinders with the equivolume diameter 20 nm and the axial ratio 1–6; Figs 7c, d show the transformation of spectra at small deviations of the particle shape from spherical.

decreases and it splits into two distinct bands. In this case, the intensity of the long-wavelength extinction band remains approximately constant, it is comparable with the short-wavelength band intensity and shifts to the red with increasing nonsphericity. The integrated scattering and absorption spectra approximately reproduce these features.

The spectra in Fig. 7c for small deviations of the particle shape from spherical are very similar to the spectra of polydisperse or weakly aggregated suspensions [89]. Thus, we come to an important conclusion that the nonsphericity and polydispersity of particles can make similar contributions to the inhomogeneous broadening and mask each other. In the given case, measurements of only scattering or extinction spectra do not allow us to distinguish these contributions. We suppose that this problem can be solved by using the unusually high depolarisation of scattered light, which was first predicted and measured for gold nanorods in [50, 203] and for silver particles in [51].

We have shown in papers [37, 50, 203, 209] that the degree of depolarisation of scattered linearly polarised laser radiation is a very sensitive parameter characterising the deviation of the particle shape from spherical. In particular, the depolarisation factor, defined by the ratio $\Delta_{vh} = I_{vh}^{sca}/I_{vv}^{sca}$ of the cross- and co-polarisation scattering intensities, for nanospheres of diameter 90 nm (original 'thiocyanate' synthesis protocol [37]) did not obey the law of increasing depolarisation for colloidal gold particles of diameters from 15 to 45 nm. The measured degree of

depolarisation (10 %) was three times lower than the expected extrapolated value, suggesting the high sphericity of particles, which was confirmed by the TEM analysis. Recently the sphericity of particles was tested by depolarisation of single-particle co- and cross-polarised scattering spectra [210].

The unexpected result of papers [50, 203] was the observation of the very high resonance depolarisation exceeding the classical limit 1/3 for dielectric particles [211, 212]. It was shown [50] that the Rayleigh depolarisation limit for PR particles was 3/4. In the limiting case, a rod gives the so-called symmetric scattering described by the expression [50, 213]

$$I = I_0^{(s)}\left[1 + |\boldsymbol{e}_s\boldsymbol{e}_0|^2 - \frac{2}{3}|\boldsymbol{e}_s^*\boldsymbol{e}_0|^2\right], \qquad (29)$$

where the constant $I_0^{(s)}$ is determined by the polarisability tensor; and $\boldsymbol{e}_0$ and $\boldsymbol{e}_s$ are the polarisation vectors of incident and scattered light. It is obvious that the depolarisation factor in the scattering plane $(\boldsymbol{k}_0, \boldsymbol{k}_s)$ is independent of the scattering angle and is 3/4. The conditions for realising symmetric scattering were analysed in detail in papers [50, 209], therefore we present here only some general results of calculations (Fig. 8), including new data obtained for silver particles. Figures 8a, b present the spectral dependences of the depolarisation factor for randomly oriented gold and silver s-cylinders with the constant diameter $2b = 15$ nm and the axial ratio $e = a/b$ varying
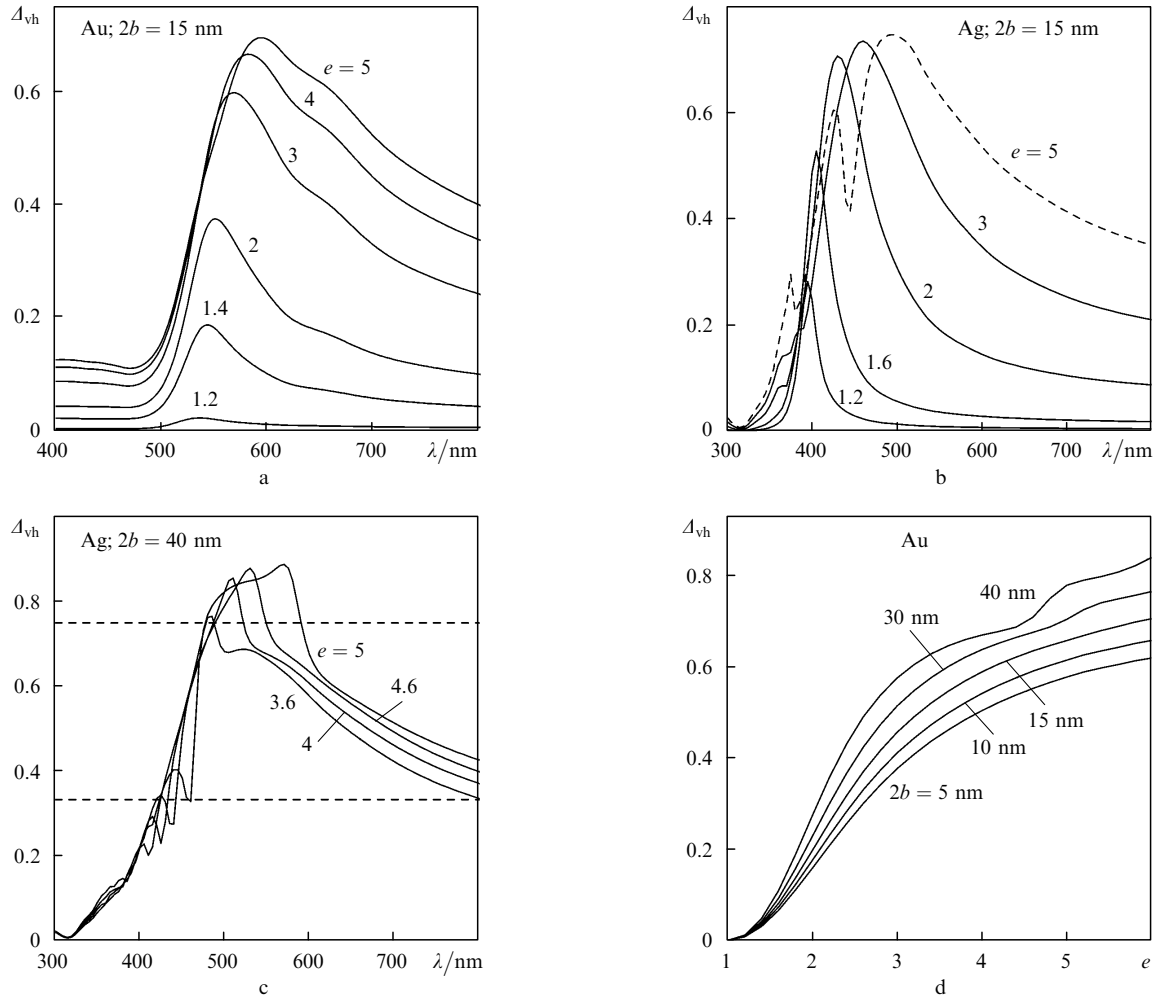
Figure 8. Spectral dependences of the depolarisation factor for randomly oriented gold (a) and silver (b, c) s-cylinders of diameter $2b = 15$ nm (a, b) and 40 nm (c) and the axial ratio e from 1.2 to 5. The dashed curves in Fig. 8c show theoretical limits for dielectric needles (1/3) and metal needles in the dipole approximation (3/4); dependence of the depolarisation factor on the axial ratio for different particle diameters ($\lambda = 633$ nm) (d).

from 1.2 to 5. It is obvious that the volume of particles under these conditions increases. The spectra for gold and silver particles are similar in that in both cases the depolarisation resonance is observed to the left of the extinction and scattering resonance [50, 51]; however, due to excitation of multipoles, the spectrum of silver particles has a more complicated structure. We present in Fig. 8c for the first time, as far as we know, an example of the violation of not only the Rayleigh depolarisation limit 1/3 for dielectric needles but also of the plasmon-resonance limit 3/4 for thin metal rods. Thick rods of diameter 40 nm with the shape factor above 3.6 have the depolarisation factor $\Delta_{vh} > 3/4$ in the wavelength range from 500 to 600 nm. It is clear that this new effect is completely caused by excitation of higher modes. Finally, Fig. 8d shows the size dependence of the depolarisation factor on the axial ratio for particles of different diameters. The curve for particles of diameter 5 nm almost does not differ from the correspondent dependence in the dipole approximation [50].

Figure 9a presents the extinction spectra for five samples synthesised by the method [32, 33] with small modifications [37] for tuning resonances in the region from 650 to 950 nm. Note that the separation stage that we introduced [203] allows us to reduce but not eliminate cubic particles and particles of nearly spherical shape (see Fig. 6 and [37]). We

found for the first time [203] the intermediate resonance at ~ 570 nm in separated samples, which was assigned based on DDA simulations [205] to cubic particles [37].

The position of the longitudinal long-wavelength resonance can be predicted from the axial ratio of particles and, vice versa, the average shape of particles can be quite accurately estimated from the resonance position. Figure 9b presents calibration dependences for measuring the axial ratio of particles from the longitudinal PR position. Along with the T-matrix calculations for s-cylinders of different diameters, we present our experimental data and data obtained by others [31, 34, 204, 214, 215]. As the particle diameter is increased, the results of a rigorous solution noticeably differ from the limiting electrostatic curve obtained in the dipole approximation (this was first shown in [50] for s-cylinders by the T-matrix method and in [204] for rectangular cylinders by the DDA method). As for the experimental data, their greater part is grouped near the curve calculated for particles of diameter 15 nm, although results [34] better agree with calculations for larger particles.

Note in conclusion that the anisotropic scattering characteristics of nanorods also determine some other interesting optical properties, in particular, the spectral and polarisation selectivity of oriented particles [34] and a strong dependence of light scattering on the orientations
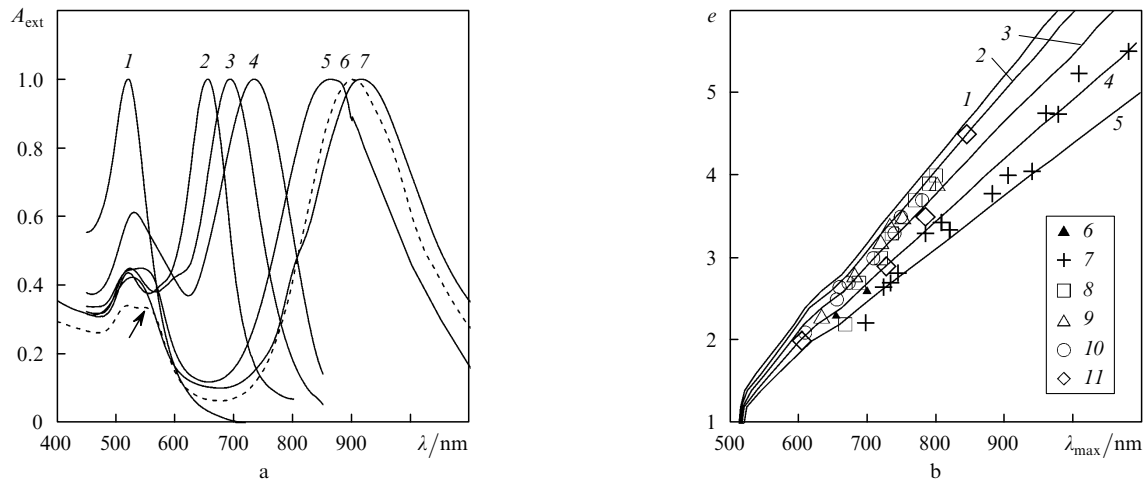
Figure 9. Normalised extinction spectra of nanorods with a longitudinal resonance at 655 (*2*), 700 (*3*), 733 (*4*), 860 (*5*), 900 (*6*), and 920 nm (*7*) [for comparison, the extinction spectrum of gold nanospheres of diameter 21 nm is shown (*1*)]; the arrow at spectrum (*6*) (dashed curve) shows the intermediate resonance of cubic particles (a); (b) calibration dependences for determining the axial ratio of particles by the longitudinal PR wavelength $\lambda_{\max}$. Calculation by the T-matrix method for randomly oriented gold s-cylinders in water, the particle diameter is 5 (*1*), 10 (*2*), 20 (*3*), 30 (*4*), and 40 nm (*5*). Experimental points are our TEM and spectral measurements (*6*) and measurements from [34] (*7*), [204] (*8*), [214] (*9*), [215] (*10*), and [31] (*11*).

of nanorods [216, 217]. Nanorods are also promising as contrasting labels in dark-field scattering microscopy [218] and coherence tomography [219]. Recently the spectral measurements of polarisation properties of individual non-spherical particles were reported [210]. It was shown that polarisation single-particle spectroscopy has a great potential for studying the interaction of nanoparticles with cancer target cells.

4.3 Gold and silver nanoshells

Gold nanoshells [2, 41, 220] and nanorods are of great interest for biosensorics [40, 49], immunoassay [221, 222], optical visualisation of biological obhects [8], and laser photodestruction of cancer cells [8, 12, 223, 224]. Note that the efficiency of nanoshells as labels for photothermolysis can be related not only to their heating but to the formation of explosive vapour bubbles [225].

The existing protocols of synthesis of gold nanoshells with a silica core [2, 41, 220, 226] allow the preparation of particles of diameter $80-400$ nm with a comparatively narrow size distribution. The resonance scattering of light by such particles exceeds by more than an order of magnitude scattering by usual colloidal gold particles of diameter from 10 to 50 nm [8]. Very strong scattering allows one to observe individual nanoshells in the dark field of a microscope [2] and opens up the way to the development of high-contrast labels for visualisation of biologically specific interactions of probe macromolecules adsorbed on particles with target molecules [227].

The optical properties of model nanoshells in the form of a bilayer sphere with a dielectric core can be easily calculated by using various programs of the Mie solution type [110, 228] or from recurrent relations for the general case of multilayer gold [229] or silver [230] spherical particles. The plasmon resonance wavelength is determined first of all by the ratio of the shell thickness to the core diameter and the dielectric functions of the core and environment. Although numerical analysis can be performed, it is desirable to have a simple analytic method for quantitative estimates of the polarisability of nanoshells
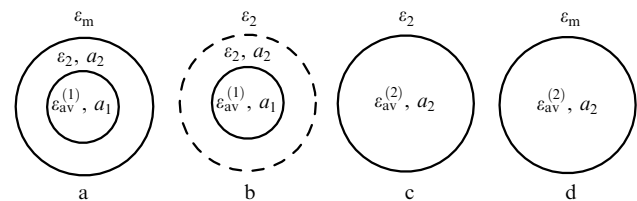

Figure 10. Scheme of the principle of the dipole equivalence: (a) the initial particle ($\varepsilon_{\mathrm{av}}^{(1)}$, a_1) covered with an external layer (ε_2, a_2) and embedded to the environment with the permittivity ε_{m}; (b) the initial particle in a medium with the permittivity ε_2 surrounded by an imaginary sphere of radius a_2; (c) an equivalent particle ($\varepsilon_{\mathrm{av}}^{(2)}$, a_2) in a medium with the permittivity ε_2; (d) an equivalent particle ($\varepsilon_{\mathrm{av}}^{(2)}$, a_2) in a medium with the permittivity ε_{m}.

and their dipole optical properties. The expression for the polarisability of bilayer particles is well known [110, 211, 212], however, it is inconvenient for practical estimates, not to mention multilayer spheres. Therefore, we proposed a new approach [49, 231] based on the principle of dipole equivalence, which consists in the following (Fig. 10).

Consider a multilayer particle of radius a_1 in a medium with the permittivity ε_{m}. We assume that its equivalent polarisability $\alpha_{\mathrm{av}}^{(1)}$, which gives the same dipole moment as that for the initial particle, is known. Then, we determine the equivalent mean permittivity $\varepsilon_{\mathrm{av}}^{(1)}$ of an equivalent homogeneous sphere by analogy with Eqn (1) as

$$\alpha_{\mathrm{av}}^{(1)} = a_1^3 \, \frac{\varepsilon_{\mathrm{av}}^{(1)} - \varepsilon_{\mathrm{m}}}{\varepsilon_{\mathrm{av}}^{(1)} + 2\varepsilon_{\mathrm{m}}}. \tag{30}$$

For a usual sphere (ε, a), we have $\varepsilon = \varepsilon_{\mathrm{av}}^{(1)} = \varepsilon_1$ and $a = a_1$. Let us now assume that a particle ($\varepsilon_{\mathrm{av}}^{(1)}$, a_1) is surrounded by an external layer of radius a_2 with the permittivity ε_2 (Fig. 10a). We will find the polarisability of such a particle from the principle of dipole equivalence. For this purpose, we will place the initial particle to a medium with the permittivity ε_2 and surround it by an imaginary sphere of

radius a_2 (Fig. 10b). Then, we replace the imaginary particle by a homogenous sphere with the equivalent permittivity $\varepsilon_{av}^{(2)}$ (Fig. 10c), which has the same dipole moment as the particle in Fig. 10b. Then, we have

$$a_1^3 \frac{\varepsilon_{av}^{(1)} - \varepsilon_2}{\varepsilon_{av}^{(1)} + 2\varepsilon_2} = a_2^3 \frac{\varepsilon_{av}^{(2)} - \varepsilon_2}{\varepsilon_{av}^{(2)} + 2\varepsilon_2}. \tag{31}$$

This equation determines the equivalent permittivity $\varepsilon_{av}^{(2)}$. Finally, if we place a new particle (Fig. 10c) to the initial medium with the permittivity ε_m (Fig. 10d), the physical situations in Figs 10a, d will be equivalent. Therefore, dipole moments will be equal, and we have the mean polarisability

$$\alpha_{av}^{(2)} = a_2^3 \frac{\varepsilon_{av}^{(2)} - \varepsilon_m}{\varepsilon_{av}^{(2)} + 2\varepsilon_m}. \tag{32}$$

It is clear that this scheme can be recurrently continued for any number of layers. For a bilayer particle, we have

$$\varepsilon_{av}^{(2)} = \varepsilon_2 \frac{1 + 2f_{12}\alpha_{12}}{1 - f_{12}\alpha_{12}}, \tag{33}$$

$$\alpha_{12} = \frac{\varepsilon_1 - \varepsilon_2}{\varepsilon_1 + 2\varepsilon_2}, \qquad f_{12} = \frac{a_1^3}{a_2^3}, \tag{34}$$

which coincides with known expressions from [110]. It is easy to verify that the method of dipole equivalence for three-layer particles also gives the same expression for the polarisability as the standard (and more cumbersome) solution of the electrostatic boundary problem. Thus, this coincidence proves the validity of the method proposed.

The main advantage of our approach is that now we can apply usual expressions for resonances of spherical particles to multilayer spheres with the equivalent permittivity as well. For example, the obvious resonance condition $\varepsilon_{av}^{(2)} = -2\varepsilon_m$ from (32) gives the resonance wavelength [49]

$$\lambda_{max} = \lambda_p(\varepsilon_{ib} + 2\varphi\varepsilon_m)^{1/2}, \tag{35}$$

$$\varphi = \frac{1}{2}\left[p_0 + \left(p_0^2 - \frac{\varepsilon_1}{\varepsilon_m}\right)^{1/2}\right],$$

$$p_0 = \frac{\varepsilon_1}{\varepsilon_m}\left(\frac{3}{4f_g} - \frac{1}{2}\right) + \frac{3}{2f_g} - \frac{1}{2} \tag{36}$$

where f_g is the volume fraction of gold in a particle. Further analysis and application of this approach to the study of the biosensoric potential of nanoshells can be found in [49]. By comparing dipole-approximation expressions (9), (28), and (35), we conclude that all they have the structure of type

$$\lambda_{max} = \lambda_p(\varepsilon_{ib} + \varphi\varepsilon_m)^{1/2} \tag{37}$$

and differ only in the form of function φ. For spheres, $\varphi = 2$, for resonances in rods, $\varphi = (L_{\parallel,\perp} - 1)$, and for shells, φ is determined by Eqn (36). We do not present here the extinction and scattering spectra of gold and silver shells for different core diameters and different metal thicknesses because, first, they often were presented in the literature [41, 220, 232, 234]. Second, the dependence of the

resonance wavelength on all parameters is qualitatively described by a simple expression [49]

$$\lambda_{max} = \lambda_p\left[\varepsilon_{ib} + \frac{3}{f_g}\left(\varepsilon_m + \frac{\varepsilon_c}{2}\right)\right]^{1/2}, \tag{38}$$

where $f_g = 1 - a_c^3/a_g^3 \approx 3\Delta a_g/a_s \ll 1$ is the volume fraction of gold in a particle with the shell thickness Δa_g and radius of a core (for example, from silicon dioxide) a_c with the permittivity ε_c. Expression (38) shows that the red shift of the resonance is observed with decreasing the relative shell thickness and increasing the refractive indices of the core and environment.

The tuning of PRs of nanorods and nanoshells is related to the shape and structure of the particles, respectively. The idea of a combination of these two particles in the form of an ellipsoidal nanoshell was proposed for the first time, as far as we know, in [232] (Fig. 11). Such a structure was later called 'nanorice' [42]. The principle of the dipole equivalence can be easily modified for such particles as well (Fig. 11). Consider two confocal spheroids with semiaxes a_1, b_1 and a_2, b_2, where $a_2^2 = a_1^2 + s^2$, $b_2^2 = b_1^2 + s^2$, and the parameter s determines the variable thickness of the shell. For polarisability along the elongated axis of a particle, Eqns (30)–(32) are replaced by

$$\alpha_{av}^{(1)} = \frac{V_1}{4\pi} \frac{\varepsilon_{av}^{(1)} - \varepsilon_m}{\varepsilon_{av}^{(1)} + (L_1^{-1} - 1)\varepsilon_m}, \tag{39}$$

$$V_1 \frac{\varepsilon_{av}^{(1)} - \varepsilon_2}{\varepsilon_{av}^{(1)} + (L_1^{-1} - 1)\varepsilon_2} = V_2 \frac{\varepsilon_{av}^{(2)} - \varepsilon_2}{\varepsilon_{av}^{(2)} + (L_2^{-1} - 1)2\varepsilon_2}, \tag{40}$$

$$\alpha_{av}^{(2)} = \frac{V_2}{4\pi} \frac{\varepsilon_{av}^{(2)} - \varepsilon_m}{\varepsilon_{av}^{(2)} + (L_2^{-1} - 1)\varepsilon_m}, \tag{41}$$

where $L_{1,2}$ are the corresponding depolarisation factors for internal and external ellipsoids. It is easy to verify that these solutions in a particular case of a bilayer ellipsoid give the known expression for polarisability [110]. Equation (41) gives the longitudinal resonance condition

$$\varepsilon_{av}^{(2)} = -\left(L_2^{-1} - 1\right)\varepsilon_m, \tag{42}$$

which contains both principles of tuning. The extinction and scattering spectra of ellipsoidal nanoshells in various dielectric media are presented in [232, 233].
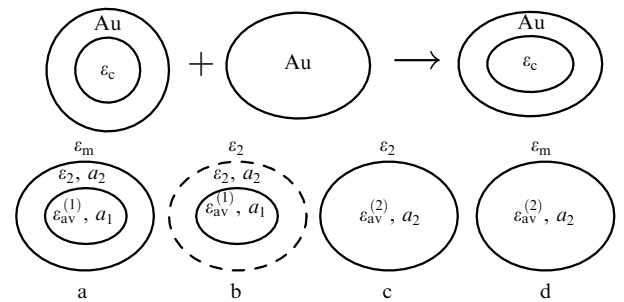

Figure 11. Scheme of the combination of a nanoshell and nanoellipse (nanorod) for obtaining an ellipsoidal nanoshell ('nanorice'). The lower scheme explains the principle of dipole equivalence for the ellipsoidal shell (see Fig. 10 caption).

The possibility of tuning of PRs of gold nanoshells [40, 41, 234, 235] and conjugation with various biopolymers allow the construction of 'multicoloured' labels based on gold nanoshells with variable structural parameters. However, the preparation of such labels is restricted by a large width of scattering spectra [usually defined as the full width at half-maximum (FWHM)] (138, 235). The typical FWHM of resonance scattering spectra of nanoshells is 150–200 nm [138] and therefore they can be used only to create two labels of different colours in the visible range and three or for labels in the visible–IR range. Except the properties of simplest nanoshells, interesting optical properties can be obtained for metal–dielectric–metal (MDM) structures, which were proposed in [235] as the base for the development of labels with very narrow resonances. However, as was shown later [138], there exists the fundamental physical restriction related to the spectral broadening due to the surface scattering of electrons on the structure boundaries [see (17)]. Figure 12 presents the integrated scattering spectra of three-layer MDM structures calculated by neglecting the surface scattering of electrons or taking it into account. The detailed analysis of results obtained in [138] shows that the line broadening in fact eliminates the advantages of three-layer structures compared to usual bilayer nanoshells. Note that, except the broadening of the resonance long-wavelength scattering peak, the restriction of the electron mean free path also considerably changes the short-wavelength part of the spectrum [see, for example, dashed curves (10) in Fig. 12].
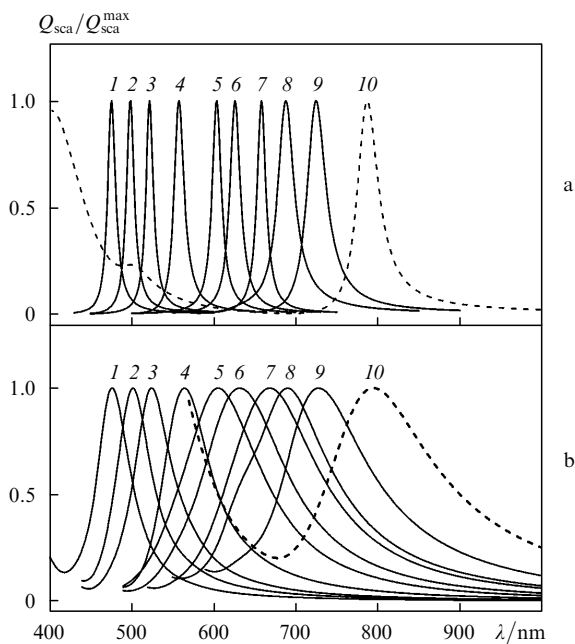
Our experiments with SiO_2/Au particles showed that the width of the spectral bands of synthesised nanoshell suspensions was always larger than the width predicted by Mie simulations of the optical properties of monodisperse bilayer particles.

The inhomogeneous broadening of the absorption spectra of gold nanoshells caused by the size dispersion and the size modification of the permittivity is well known [155]. The influence of the polydispersity structure of gold nanoshells and the restriction of the electron mean free path in a thin metal layer on the resonance scattering spectra of the suspension of bilayer nanoparticles was studied theoretically and experimentally in [156]. The calculations showed that both these factors lead to the broadening of the scattering
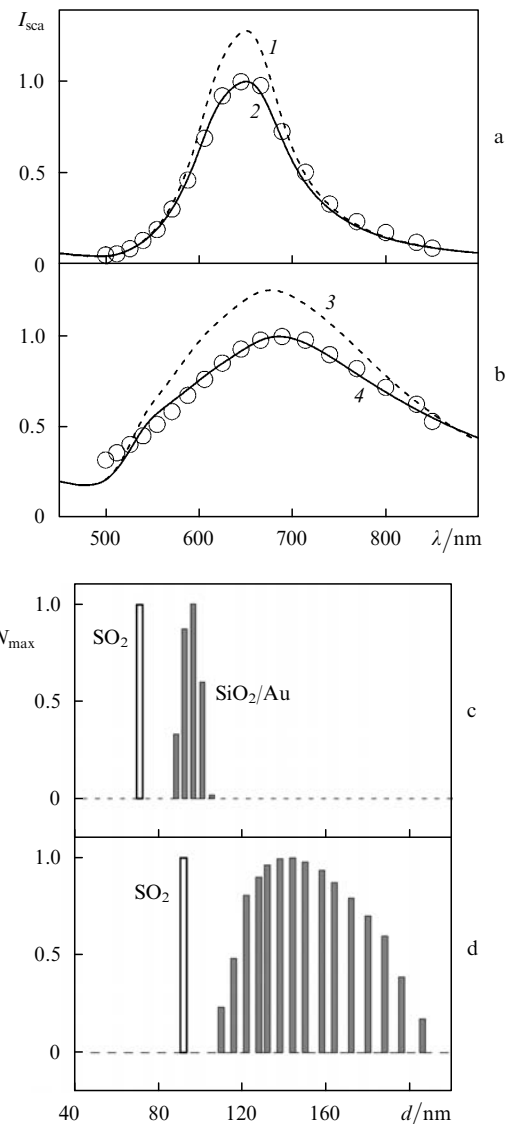
Figure 12. Normalised integrated scattering spectra calculated from volume optical constants of metals (a) and taking into account the surface scattering of electrons (b). The figures at the curves denote the MDM structure parameters in nanometers: core radius/core material/ shell 1 thickness/shell 1 material/ shell 2 thickness/ shell 2 material: (1) 2.5/Ag, 4/SiO$_2$, 3.5/Ag; (2) 3.25/Ag, 3.25/SiO$_2$, 3.5/Ag; (3) 3.5/Ag, 3.5/ SiO$_2$, 3/Ag; (4) 4.25/Ag, 2.75/SiO$_2$, 3/Ag; (5) 4/Ag, 4/SiO$_2$, 2/Ag; (6) 4.5/Ag, 2.5/SiO$_2$, 2/Ag; (7) 5/Ag, 3/SiO$_2$, 2/Ag; (8) 4.75/Ag, 2.75/SiO$_2$, 2.5/Au; (9) 5.25/Ag, 2.25/SiO$_2$, 2.5/Au; (10) 5.75/Ag, 1.75/SiO$_2$, 2.5/ Au.

Figure 13. Normalised experimental (points) and theoretical (curves) scattering spectra for samples (1) (a) and (2) (b) and the corresponding histograms of the distribution of SiO$_2$ particles and SiO$_2$/Au nanoshells over diameters for samples (1) (c) and (2) (d). Theoretical curves are calculated for particles with the core diameter 71 (1, 2) and 90 nm (3, 4) and a monodisperse gold shell of thickness 15 (1, 2) and 30 nm (3) by neglecting the restriction of the electron mean free path (1, 3, 4) and taking it into account (2), and also taking into account the gold-shell thickness distribution (4). The calculated spectra (1, 2) and (3, 4) are normalised to the maxima of curves (2) and (4), respectively.

PR and a change in its maximum. Calculations were verified for two synthesised samples of gold SiO_2/Au nanoshells with a core diameter of 71 nm and a narrow shell-thickness distribution [the average distribution width was 15 nm, sample (*1*) in Fig. 13] and a core diameter of 180 nm and a broad shell-thickness distribution [of width 30 nm, sample (*2*) in Fig. 13]. The size of the core, thickness, and polydispersity of nanoparticle strictures were estimated by the method of dynamic light scattering (DLS). The simulation of the optical properties of nanoparticles with parameters based on the DLS data gives good agreement with experimental spectra (Fig. 13). In the case of samples of type (*1*), the spectral broadening was mainly determined by the restriction of the electron mean free path, while the shell-thickness distribution could be neglected. The inhomogeneous broadening of the scattering spectrum of sample (*2*) was mainly determined by the polydispersity, and spectra could be simulated by using the volume constants for gold. These experiments showed that to study the mechanisms of spectral broadening, it is preferable to measure the single-particle scattering spectra of nanoshells, as was done in [167].

Along with the above-considered effects, another factor affecting the spectral broadening is the rough structure of shells. Figure 14 presents the image of nanoshells obtained in a scanning electron microscope. One can see that the reduction of gold on initial seeds leads to the formation of an uneven surface. The influence of various types of nanoshell inhomogeneities on extinction spectra was carefully studied in [180]. It was found that this effect enhanced the short-wavelength and long-wavelength extinction and caused the broadening of the spectrum.
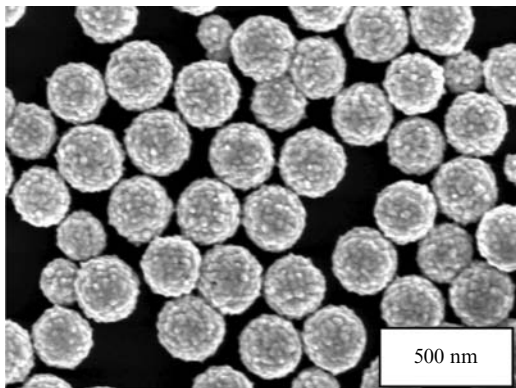

Figure 14. Scanning electron microscope image of SiO_2/Au shells of size 210/15 nm.

4.4 Optimisation of properties of particles for biosensorics

The problem of optimisation of the sensitivity of a conjugate to variations in the local dielectric environment was theoretically studied for gold [228, 229] and silver [230] nanoparticles and for SiO_2/Au nanoshells covered with an inhomogeneous polymer layer [49, 236]. The dependence of the PR on the dielectric environment can be qualitatively understood from general expression (37). A small change Δn_m in the refractive index of the environment will cause the spectral shift of the resonance, which is described by the universal expression [37]

$$\frac{\Delta \lambda_{max}}{\lambda_{max}} = \frac{\Delta n_m}{n_m} \left(1 - \frac{\lambda_0^2}{\lambda_{max}^2} \varepsilon_{ib} \right). \tag{43}$$

A remarkable property of this expression is that all the parameters of particles enter it in the universal way via the resonance wavelength, while the material properties determine only two parameters: the plasma wavelength and the contribution of interband transitions to the dielectric function. We obtain a simple approximate rule according to which the relative resonance shift is proportional to a relative change in the refractive index of the medium with the proportionality coefficient ~ 0.5. Expression (43) was verified in our experiments with glycerol suspensions of nanorods [37] and by data [214]. Another approach to the analytic study of the biosensoric potential of various particles was developed in [237].

Let us discuss briefly data for spheres and nanoshells. Figure 15 shows the model of a conjugate with a metal core, primary shell 1 with probing molecules (1-PM) and secondary shell 2 with target molecules (2-TM). The inhomogeneous structure of each shell can be simulated by an arbitrary number of homogenous layers (Fig. 15 shows the case with two layers for each shell). As optimisation parameters, we used the absolute changes in the optical density and scattering intensity of conjugates with the primary shell (subscript 1) and after the attachment of target molecules (subscript 2):

$$\Delta A_{21}(\lambda) = A_2(\lambda) - A_1(\lambda), \quad \Delta I_{21}(\lambda) = I_2(\lambda) - I_1(\lambda). \tag{44}$$

The maximum sensitivity of extinction to the formation of the adsorption layer of molecules is observed for gold particles of diameter $40-50$ nm and silver particles of
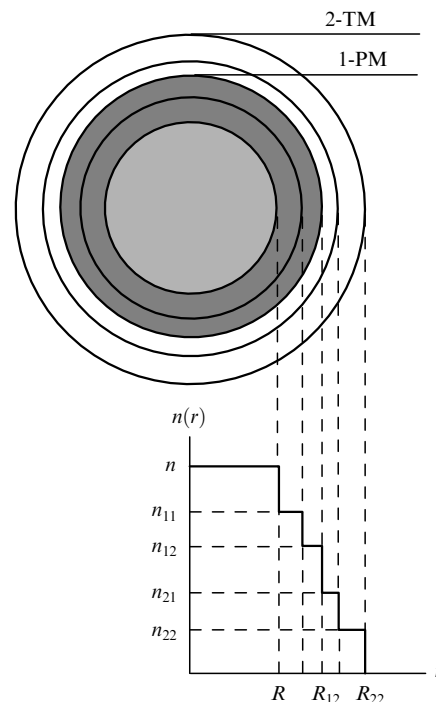

Figure 15. Model of a conjugate with a metal core, primary shell 1 with probing molecules (1-PM) and secondary shell 2 with target molecules (2-TM). The inhomogeneous structure of each shell is simulated by an arbitrary number of homogeneous layers.
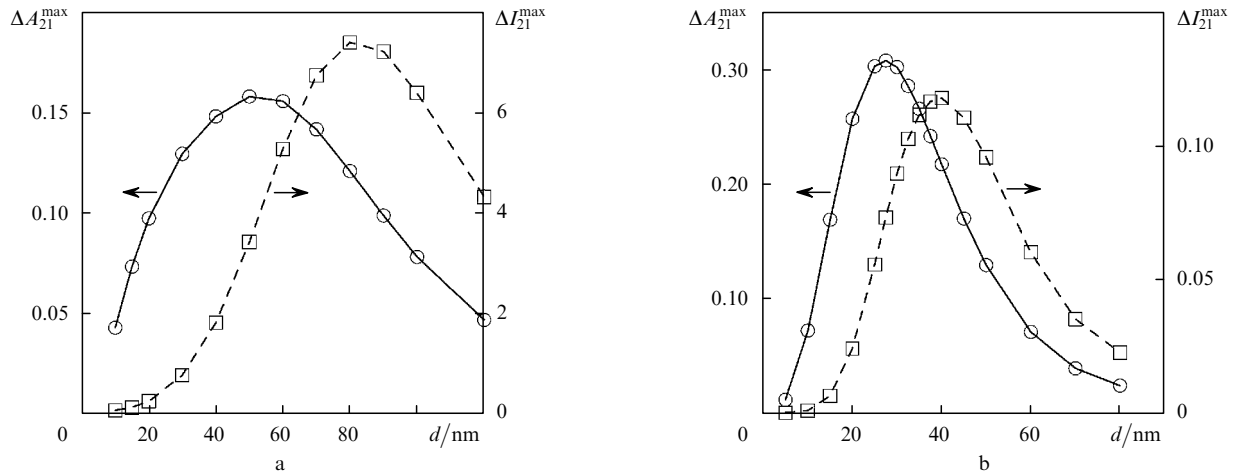
Figure 16. Dependences of changes in the extinction (ΔA_{21}^{max}) and scattering (ΔI_{21}^{max}) maxima on the diameter of gold (a) and silver (b) particles. The calculation parameters are: thickness of layers of the primary shells $s_{11} = s_{12} = 2.5$ nm, refractive indices $n_{11} = 1.50$ and $n_{12} = 1.45$, thickness of layers of the secondary shell $s_{21} = 2$ nm, $s_{22} = 3$ nm, refractive indices $n_{21} = 1.45$ and $n_{22} = 1.40$ (see Fig. 15).

diameter ~ 30 nm (Fig. 16). In the case of measuring scattering, the corresponding maxima of the curves are observed for particle diameters 80 and 40 nm. The dependence of the PR shift is described by the universal function of the ratio of the layer thickness to the particle size, which was obtained independently in [228, 238]. Experimental data on the size optimisation of the PR sensitivity to the dielectric environment were published in [97, 239] and confirmed as a whole the conclusions of our analysis.

The biosensoric potential of gold nanoshells was studied in [49]. At first glance it seems that the PR of nanoshells should be considerably more sensitive to changes in the dielectric environment. However, contrary to expectations, the difference between homogeneous particles and nanoshells proved to be not too large. Calculations of the differential spectra $\Delta A_{12}(\lambda)$ and $\Delta I_{12}(\lambda)$ have shown that as a whole changes in extinction and scattering for particles of both types are approximately comparable and these spectra can be used for detecting biospecific interactions on the surface of particles. The maximum sensitivity to the

formation of a layer of target molecules was found for the ratio of a metal shell thickness to its external radius in the range 0.2–0.4.

The data on variations in PR extinction and scattering for several equivolume models, including spheres, spherical and elliptic nanoshells, nanorods in the form of ellipsoids and s-cylinders and also bispheres were compared for the first time in papers [232–234]. The latter model was chosen because of the presence of a particular contact point in which the field of interacting particles is very strong and strongly inhomogeneous. Figure 17 presents the generalised results of calculations, which leads to the following conclusions. For nanoparticles with the equivolume diameter 15–60 nm, the maximum PR shifts with changing the refractive index of the environment are observed for bispheres or ultrathin (2 nm) shells and decrease in a series bispheres–nanoshells–s-cylinders (spheroids)–spheres. As the thickness of particles is increased, their sensor properties approach those of spheres. The resonance of silver nanoparticles is more sensitive to the dielectric environment.
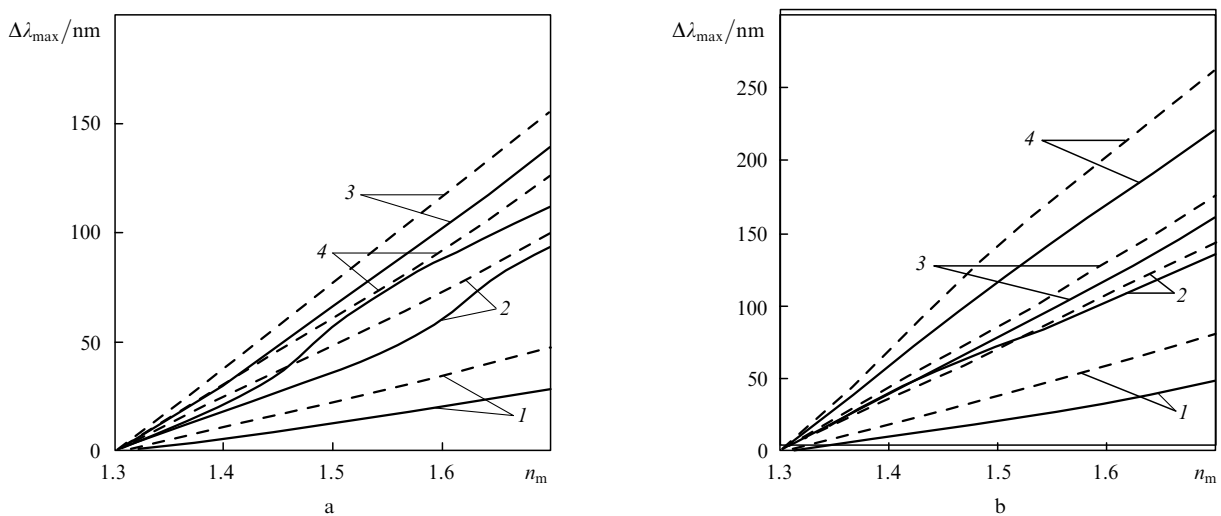

Figure 17. Dependences of the spectral shift of the resonance of gold (solid curves) and silver (dashed curves) nanoparticles on the refractive index of the environment; (1) spheres; (2) spheroids; (3) bispheres with the equivolume diameter 15 (a) and 60 nm (b); (4) nanoshells of thickness $s = 2$ nm with the internal cavity diameter 15 (a) and 60 nm (b).

5. Multipole resonances in metal nanorods

Compared to numerous data on the dipole properties of nanorods published in the last years, the studies of multipole resonances are quite limited. As far as we know, the first study of quadrupole modes was performed for silver spheroids and nanolithographic 2D structures [240]. Quadrupole modes were also investigated for silver [111] and gold spheroids, circular and s-cylinders, and rectangular prisms [52, 53]. Quadrupole resonances were also identified based on DDA simulations and experimental measurements of silver [241] and gold [54] nanoprisms. Recently the first observations of multipole PRs in silver nanowires on a dielectric substrate [242, 243] and colloidal gold nanorods [55] were reported.

Multipole resonances were interpreted and assigned based on the conception of standing waves [244–247] and DDA calculations [111]. However, the DDA algorithm does not contain the multipole representation in the explicit form because a particle is treated as a set of interacting point dipoles. By using the T-matrix method, we studied in detail this problem, derived the rule for partial contributions and determined the influence of light polarisation, orientation of particles and dielectric environment on the excited resonances [56]. We showed for the first time that the dependence of resonance wavelengths on the axial ratio divided by the resonance number for particles of different sizes and shapes is described by the universal scaling linear law. The optimal orientation and polarisation configurations for excitation of certain dipoles were established. In particular, the conclusion obtained in [52, 53] was confirmed that a quadrupole resonance can be excited only in the TM polarisation, the excitation being most efficient when the symmetry axis makes an angle of $53-54°$ with respect to the wave vector. In this review, we present a brief summary of the most important results. The detail study of the quadrupole resonance in nanorods is presented in our papers [52, 53].

The multipole representation of the normalised extinction, scattering and absorption cross sections in the T-matrix method is given by the expression

$$Q_{\text{ext,sca,abs}} = \sum_{l=1}^{N} q_{\text{ext,sca,abs}}^{l}. \tag{45}$$

For randomly oriented particles, we obtain from averaging expressions [158, 248]

$$q_{\text{ext}}^{l} = \frac{2}{k^2 R_{\text{ev}}^2} \, \text{Spur}_l(T_{\sigma\sigma}), \tag{46}$$

where $\sigma \equiv (l, m, p)$ is the T-matrix multisubscript (order, degree, and mode) and the trace is taken over all subscripts except l. The basic scattering geometry for axially symmetric particles is shown in Fig. 18. The spectral resonances are numbered according to the rule $Q_{\text{ext}}^{n} \equiv Q_{\text{ext}}(\lambda_n)$ ($n = 1, 2, 3, \ldots$, from the IR to visible range) and the symbol '0' refers to the shortest-wavelength resonance. Note also that the first (dipole) resonance for our particles is usually located far in the IR range.

It follows from Fig. 18 the longest-wavelength resonance for randomly oriented particles corresponds to the dipole TM mode ($n = 1$), while the short-wavelength ('zero') resonance corresponds to the TE excitation. The scattering
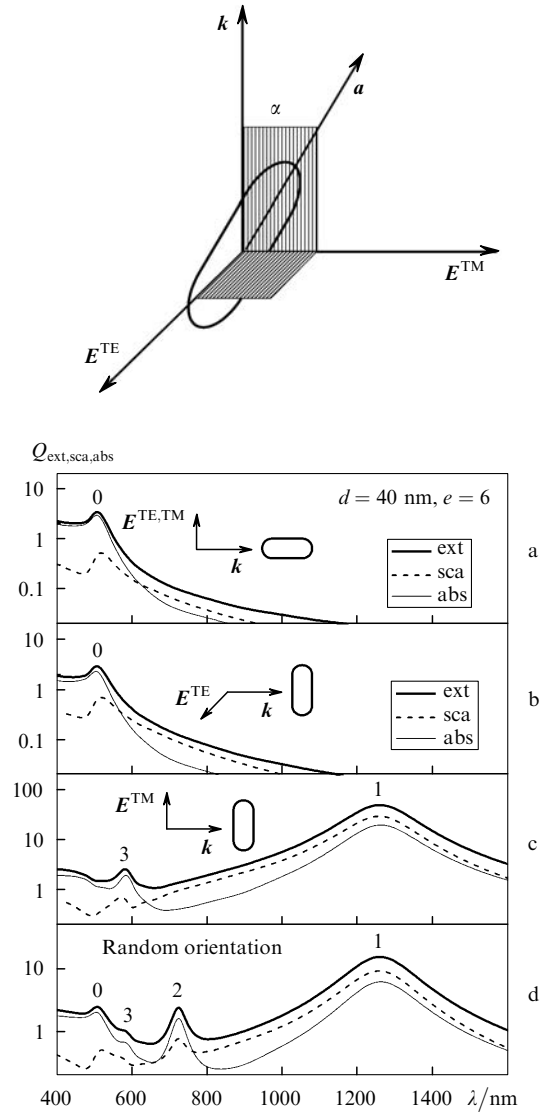

Figure 18. Fundamental TE and TM polarisations of the incident light. The orientation of particles is specified by the angle α between the wave vector $\boldsymbol{k}$ and the symmetry axis $\boldsymbol{a}$ of a particle. Below: the extinction, absorption, and scattering spectra of a gold rod for longitudinal (a), transverse TE- (b), perpendicular TM- (c), and random (d) orientation of particles with respect to the incident polarised light. The figures at the curves indicate the resonance number.

and absorption resonances are of the same order of magnitude, have the same wavelength, and give comparable contributions to extinction for particles considered in this case. Finally, for basic longitudinal or transverse orientations, some multipoles are symmetry-forbidden (for example, the quadrupole resonance $n = 2$ in Figs 18a–c and the third resonance in Figs. 18a, b). The spectra of randomly oriented particles contain most complete information on all possible excitation configurations and, therefore, they are most interesting along with fixed orientations.

The extinction spectra $Q_{\text{ext}}(\lambda)$ of randomly oriented rods with the minor axis $d = 80$ nm and the axial ratio $e = 10$ are shown in Fig. 19. Except the usual long-wavelength longitudinal resonance (not shown), five additional resonances are distinctly observed (the sixth resonance looks like a weak shoulder, but it is distinctly seen in curve q_6). Of
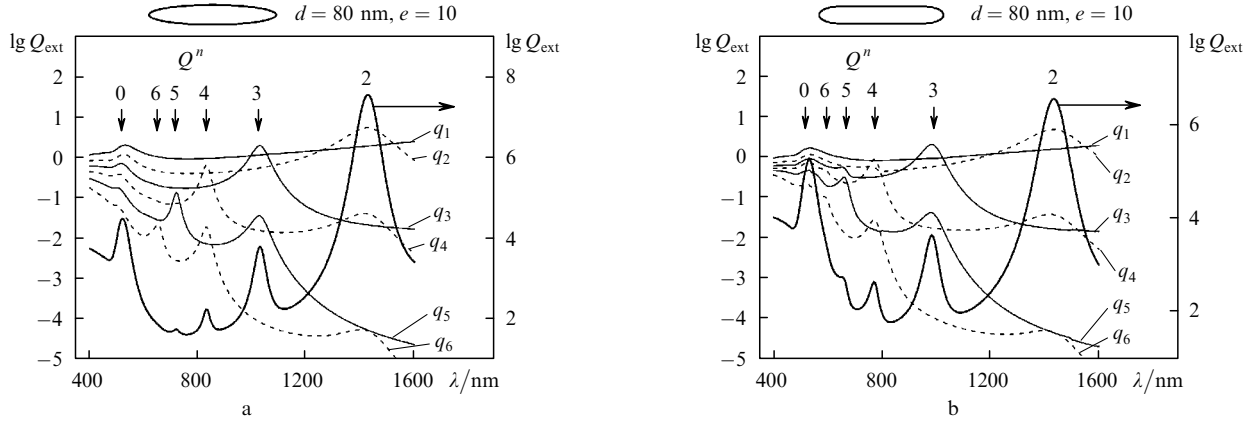
Optics and biophotonics of nanoparticles with a plasmon resonance

Figure 19. Extinction spectra $Q_{ext}(\lambda)$ of randomly oriented gold spheroids (a) and s-cylinders (b) of diameter $d = 80$ nm and the axial ratio $e = 10$. Curves $q_1 - q_6$ show the spectra of multipole contributions; numbers $n = 1 - 6$ denote resonances $Q^n = q_{ext}(\lambda_n)$. The first resonance Q^1 localised in the far-IR region is not shown. The zero resonance is the sum of multipoles rather than purely dipole excitation, although it is localised near the dipole TE mode.

course, the exact position of resonances depends on the shape and size of particles. For example, five resonances ($n = 6 - 2$) for spheroids are located at $\lambda_{6-2} = 655, 720, 832, 1030$, and 1428 nm, and for s-cylinder at $590, 655, 770, 985$, and 1332 nm.

The analysis of spectra in Fig. 19 leads to the following conclusions: (i) the parity of the general resonance coincides with that of multipole contributions; (ii) for the given resonance number n, the number l of a partial contribution is equal to or exceeds n:

$$Q^{2n} = \sum_{l \geqslant n} q_{2l}(\lambda_{2n}), \quad Q^{2n+1} = \sum_{l \geqslant n} q_{2l+1}(\lambda_{2n+1}). \quad (47)$$

This means that the dipole resonance q_1 does not contribute to resonances $Q^{2n+1} (n \geqslant 1)$, the quadrupole q_2 does not contribute to resonances $Q^{2n} (n \geqslant 1)$, etc. Although the parity rule (47) is valid for all three shapes of particles that we studied, the second statement ($l \geqslant n$) depends, generally speaking, on the particle shape. We omit here the detailed study of the dependence of these effects on the volume,

axial ratio, and orientation of particles, which was performed in our paper [56]. In conclusion of this section, we present only the scaling law for multipole resonances (Fig. 20).

It is well known [31] that the wavelength of a dipole longitudinal resonance depends on the axial ratio almost linearly, the slope of the straight line being weakly dependent on the volume of small particles (see also Fig. 9b). However, this slope for multipole resonances strongly depends on the axial ratio [54]. The question arises of whether the wavelengths of multipole resonances obey any scaling. To answer this question, we studied the extinction, scattering and absorption spectra of particles of diameters $d = 20, 40$, and 80 nm and the axial ratio in the range $2 - 20$. To our surprise, we found that some resonances for some values of e had the same wavelengths, the ratio e/n being constant. We assumed the presence of the universal scaling of the form

$$\lambda_n = f\left(\frac{e}{n}\right) \simeq A_0 + A\frac{e}{n}, \quad (48)$$
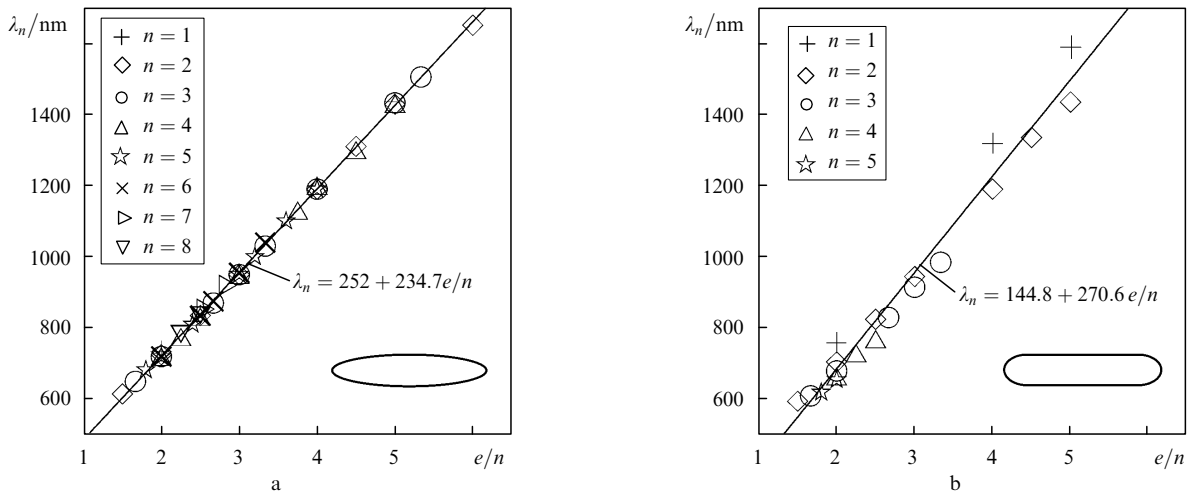
Figure 20. Linear scaling for the wavelengths λ_n of dipole resonances as a function of the normalised axial ratio e/n. The calculation is performed for randomly oriented spheroids (a) and s-cylinders (b) in water. The particle diameter is $d = 80$ nm, the axial ratio is $e = L/d = 2 - 20$. The number of observed resonances changes from five to eight depending on the particle shape. Linear approximation equations are presented in figures.

where constants A_0 and A are independent of the resonance number. It follows from Fig. 20 that this assumption is completely confirmed by numerical calculations. The scaling law (48) can be physically explained based on the dispersion law obtained for standing plasmon waves [244–247]:

$$n \frac{\pi}{L} = \frac{2\pi}{\lambda_n^{\text{eff}}} = q^{\text{eff}}(\omega_n), \tag{49}$$

where $q^{\text{eff}}(\omega_n)$ is the effective wave number corresponding to the resonance frequency ω_n. For a constant diameter d of particles, Eqn (49) predicts a linear scaling $\lambda_n^{\text{eff}} \sim L/n \sim de/n \sim e/n$, in accordance with Eqn (48) and our calculations. We showed in paper [56] that the multipole resonances of rods in media with different refractive indices shifted according to linear scaling (43). This result is somewhat unexpected because initial expression (43) was obtained in the dipole approximation.

6. Applications in biophotonics

For the last decade, PR particles were not only an object of extensive physicochemical studies but were also investigated from the point of view of potential applications in biosensorics and biomedicine. The high sensitivity of PRs to the local dielectric environment and, especially, to the presence of other resonance scatterers in the near field gives information on the bimolecular coupling or distribution of biolmolecules near a highly sensitive particle, in particular, on single-molecule coupling [210, 249]. The most attractive properties of gold nanoparticles are their high stability, chemical inertness and biocompatibility, the absence of photobleaching, and a comparatively simple functionalisation by biomolecules.

At a new stage of the development of nanobiotechnology, even old methods acquire the 'second breath'. A new immunoassay method, called by the authors [92] the sol particle immunoassay (SPIA), was proposed as early as 1980. The method is based on the detection of variations in the absorption spectrum of a sol following the biospecific aggregation of nanoparticles [250]. This method was recently efficiently applied [251] for diagnostics of tuberculosis by using samples taken from patients after one stage of a polymerase chain reaction. In a more general aspect, SPIA is a convenient and simple test for detecting polymorphism or mutations at the level of several bases in an oligonucleotide being analysed [252]. Recently SPIA was combined with dynamic scattering by using combinations of nanosphere and nanorod conjugates and combination of conjugates of nanospheres and nanorods were used to form biospecific aggregates [253].

The second example of such a renaissance is solid-phase immunoassay [254] in which target molecules or antigens are adsorbed on a solid carrier and then are revealed with the help of various labels conjugated with recognising probing molecules. Among a variety of methods of solid-phase analysis, of special interest is the so-called dot analysis based on the specific staining of a sample drop adsorbed on a membrane [255] or other substrate. The main advantage of this method is that analysis does not require the expensive equipment and means for signal processing. Tests can be performed even at home or under field conditions, unlike, for example, solid-phase analysis with the use of scanning

atomic-force microscopy [256, 257], scanning technology of laser-induced scattering near a heated metal nanoparticle [258] or single-particle resonance light scattering [259]. An example can be the known tests for pregnancy at the early stage or tests for the presence of narcotics and toxins in the human blood.

In the dot analysis, the minimal volumes of solutions of target molecules are applied on a substrate in the form of a series of dots, which allows a considerably greater number of analyses to be performed with the same amount of reagents compared, for example, to immunoenzyme assay (ELISA). The most popular sorbents for solid-phase membrane immunoassay are nitrocellulose and its modifications [260], although silicon-doped matrices [261] or microscopic functionalised glass arrays [262], which can be constructed in the form of biochips [263, 264], are also used at present. The attachment of proteins or other biomacromolecules with a membrane occurs mainly due to electrostatic interactions [265]. Almost a quarter of century ago several groups independently proposed to use colloidal gold as a label for solid-phase immunoassay [266] in which the intense colour of the label allows the visual observation of the result of a reaction performed on a solid carrier. Detailed information on the principles, technology and biological and medical applications of immunogold dot analysis is contained in recent review [10].

Due to the use of functionalised gold nanoparticles and the technology of silver enhancement in the last years [262, 267], the sensitivity of dot analysis was increased to 1 pg of IgG molecules immobilised on a glass or to the concentration of IgG molecules in solutions down to 2.75 ng mL^{-1} [268]. Also, the record atto- and zepto-molar sensitivities of various variants of solid-phase analysis were reported [269] (comparable with the limiting sensitivity of resonance scattering [259]). The method was developed by combining PR particles with enzymes [270], peptides [271], fluorescent labels [272], chitosans [273], and by using gold particles with a magnetic core, which provided the limiting sensitivity of ~ 0.14 ng mL^{-1} [274]. By using the standard protocol of dot analysis on a nitrocellulose membrane with colloidal gold particles of diameter 15 nm as labels, we showed [2, 222] that the minimal detected amount of rabbit IgG was 15 ng, while the replacement of particles of diameter 15 nm by nanoshells improved the analysis sensitivity by almost an order of magnitude. Recent, more detailed studies performed in our laboratory showed [275] that the replacement of colloidal gold conjugates by nanoshells improved the analysis sensitivity to 0.2 ng in the case of nanoshells of sizes 180/15 nm and to 0.4 ng for nanoshells of sizes 100/15 and 140/15 nm. By using the developed theory, we explained the dependences of the detection threshold, the sensitivity range of the method, the maximum staining, and the probe-amount saturation threshold on the parameters of particles.

One of the most promising applications of PR particles in biology is the visualisation of target molecules in tissues or cells by the method of resonance scattering [7, 8, 276]. This method is based on the fact that the intensity of light scattered by metal particles conjugated with probing molecules exceeds the fluorescence intensity of labels approximately by five orders of magnitude. At other stages, the detection, say, of a deffect in the gene sequence of nucleotides does not differ from standard procedures using oligonucleotides with fluorescent labels [277].

A new technology based on two-photon luminescence (TPL) of metal nanoparticles was developed recently. An obvious advantage of TPL over usual dark-field microscopy is selective excitation of only target particles, which excludes elastic scattering from nonresonance impurities. The physical mechanism of excitation can be qualitatively described as follows [278]. The first photon excites an electron during the interband transition from the sp conduction band below the Fermi level to the sp band above the Fermi level and forms a hole in the first band. This transition is polarisation-dependent and is efficient for nanorods only in the case of longitudinal polarisation. The second photon excites a d electron to the lower sp band, where the first photon has formed the hole. This transition is independent of polarisation. The recombination of the electron and hole results in the emission of a luminescence photon.

The combination of TPL with confocal microscopy gives the unique possibility to observe and distinguish PR labels on the surface of and inside cells. It was shown recently that the resonance TPL of nanorods [279, 280] and nanoshells [281] had the single-particle intensity sufficient for the use of these labels as contrast agents for the visualisation of cancer molecular markers and investigations of intracellular processes. It was shown [282] that usual functionalised gold nanospheres could be used for the TPL visualisation of particles on the surface of and inside cancer cells.

Strong resonance absorption in nanoparticles is used in photoacoustic visualisation [283, 284] and photothermolysis of cancer cells (see references in [14] and review [13]). The first method is based on the generation of acoustic waves upon pulsed heating of particles, which allows the acoustic monitoring of the particle movement, for example, in blood vessels. The second method is based on the specific labelling of cancer cells by conjugates of nanoparticles with antibodies against a molecular cancer antigen. The subsequent irradiation by laser pulses leads to a rapid local heating of particles due to resonance absorption, which causes eventually the damage of only labelled cells, leaving healthy cells undamaged. The damage mechanisms are now being investigated. Apart from PR particles, the photothermolysis of cancer cells was also produced by using hybrid particles combining magnetic and PR properties [285].

The interesting applications of metal nanoparticles are also expected for the directional delivery of substances to biological targets [9, 120], which is based on the selective size-dependent penetration of particles into living cells [286] and their selective distribution in living organisms [287].

7. Conclusions

The daily updated list of publications on PR particles often brings unexpected variants of their applications. We conclude this review by the reference to two papers published in the January issue of Nature, 2008, which are devoted to the creation of artificial single crystals based on nanoparticles conjugated with oligonucleotides [288, 289]. These publications are quite symbolic. First, the two research groups have simultaneously obtained an outstanding result under conditions of a severe temporal competition. Second, this demonstrates again the unpredictable possibilities of nanobiotechnology and biophotonics based on the use of new building PR particle – molecule blocks.

8. References

1. Cheng M.M., Cuda G., Bunimovich Y.L., Gaspari M., Heath J.R., Hill H.D., Mirkin C.A., Nijdam A.J., Terracciano R., Thundat T., Ferrari M. *Curr. Opin. Chem. Biol.*, **10**, 11 (2006).
2. Khlebtsov N.G., Bogatyrev V.A., Dykman L.A., Khlebtsov B.N. *Ross. Nanotekhnol.*, **2**, 69 (2007).
3. Lakowicz J.R. *Plasmonics*, **1**, 5 (2006).
4. Stuart D.A., Haes A.J., Yonzon C.R., Hicks E.M., Van Duyne R.P. *IEE Proc. Nanobiotechnol.*, **152**, 13 (2005); Wei A. *e-J. Surf. Sci. Nanotech.*, **4**, 9 (2006); Stewart M.E., Anderton C.R., Thompson L.B., Maria J., Gray S.K., Rogers J.A., Nuzzo R.G. *Chem. Rev.*, **108**, 494 (2008).
5. Rosi N.L., Mirkin C.A. *Chem. Rev.*, **105**, 1547 (2005).
6. Kumar S., Harrison N., Richards-Kortum R., Sokolov K. *Nano Lett.*, **7**, 1338 (2007).
7. El-Sayed I.H., Huang X., El-Sayed M.A. *Nano Lett.*, **5**, 829 (2005).
8. Loo C., Hirsch L., Lee M., Chang E., West J., Halas N., Drezek R. *Opt. Lett.*, **30**, 1012 (2005).
9. Paciotti G.F., Kingston D.G.I., Tamarkin L. *Drug Dev. Res.*, **67**, 47 (2006).
10. Dykman L.A., Bogatyrev V.A. *Usp. Khim.*, **76**, 199 (2007) [*Rus. Chem. Rev.*, **76**, 181 (2007)].
11. Huang X., El-Sayed I.H., Qian W., El-Sayed M.A. *J. Am. Chem. Soc.*, **128**, 2115 (2006).
12. Pissuwan D., Valenzuela S.M., Cortie M.B. *Trends Biotechnol.*, **24**, 62 (2006).
13. Jain P.K., El-Sayed I.H., El-Sayed M.A. *Nano Today*, **2**, 18 (2007).
14. Khlebtsov B.N., Zharov V.P., Melnikov A.G., Tuchin V.V., Khlebtsov N.G. *Nanotechnology*, **17**, 5267 (2006).
15. Kreibig U., Vollmer M. *Optical Properties of Metal Clusters* (Berlin: Springer-Verlag, 1995).
16. Glomm W.R. *J. Disp. Sci. Tech.*, **26**, 389 (2005).
17. Schultz D.A. *Curr. Opin. Biotechnol.*, **14**, 13 (2003).
18. Cang H., Sun T., Li Z-Y., Chen J., Wiley B.J., Xia Y. *Opt. Lett.*, **30**, 3048 (2005).
19. Pitsillides C.M., Joe E.K., Wei X., Anderson R.R., Lin C.P. *Biophys. J.*, **84**, 4023 (2003); Zharov V., Galitovsky V., Viegas M. *Appl. Phys. Lett.*, **83**, 4897 (2003); Hirsch L.R., Stafford R.J., Bankson J.A., Sershen S.R., Rivera B., Price R.E., Hazle J.D., Halas N.J., West J.L. *Proc. Natl. Acad. Sci. USA*, **23**, 13549 (2003).
20. Liao H., Nehl C.L., Hafner J.H. *Nanomedicine*, **1**, 201 (2006).
21. Khlebtsov N.G., Maksimova I.L., Tuchin V.V., Wang L., in *Handbook of Optical Biomedical Diagnostics*. Ed. by V.V. Tuchin (Bellingham: SPIE, 2002) Ch. 1, pp 31–167.
22. Khlebtsov N.G., Melnikov A.G., Dykman L.A., Bogatyrev V.A., in *Photopolarimetry in Remote Sensing*. Ed. by G. Videen, Ya.S. Yatskiv, M.I. Mishchenko (Dordrecht: Kluwer, 2004) pp 265–308.
23. Lee K.-S., El-Sayed M.A. *J. Phys. Chem. B*, **109**, 20331 (2005).
24. Jain P.K., Lee K.S., El-Sayed I.H., El-Sayed M.A. *J. Phys. Chem. B*, **110**, 7238 (2006).
25. Noguez C.J. *J. Phys. Chem. C*, **111**, 3806 (2007).

26. Hayat M.A. (Ed.) *Colloidal Gold: Principles, Methods and Applications* (San Diego: Acad. Press, 1989) Vol. 1, Vol. 2; 1990, Vol. 3.

27. Daniel M.-Ch., Astruc D. *Chem. Rev.*, **104**, 293 (2004).

28. Xia Y., Halas N.J. *MRS Bulletin*, **30**, 338 (2005).

29. Yu Y.-Y., Chang S.-S., Lee C.-L., Wang C. R. Ch. *J. Phys. Chem. B*, **101**, 661 (1997).

30. Chang S.-S., Shih C.-W., Chen C.-D., Lai W.-C., Wang C.R.Ch. *Langmuir*, **15**, 701 (1999).

31. Link S., El-Sayed M.A. *J. Phys. Chem. B*, **103**, 8410 (1999).

32. Jana N.R., Gearheart L., Murphy C.J. *J. Phys. Chem. B*, **105**, 4065 (2001).

33. Nikoobakht B., El-Sayed M.A. *Chem. Mater.*, **15**, 1957 (2003).

34. Pérez-Juste J., Pastoriza-Santos I., Liz-Márzan L.M., Mulvaney P. *Coordination Chem. Rev.*, **249**, 1870 (2005).

35. Murphy C.J., Sau T.K., Gole A.M., Orendorff C.J., Gao J., Gou L., Hunyadi S.E., Li T. *J. Phys. Chem. B*, **109**, 13857 (2005).

36. Liz-Marzán L.M. *Langmuir*, **22**, 32 (2006).

37. Alekseeva A.V., Bogatyrev V.A., Khlebtsov B.N., Mel'nikov A.G., Dykman L.A., Khlebtsov N.G. *Kolloid. Zh.*, **68**, 725 (2006) [*Colloid J.*, **68**, 661 (2006)].

38. Oldenburg S., Averitt R.D., Westcott S., Halas N.J. *Chem. Phys. Lett.*, **288**, 243 (1998).

39. Sun Y., Xia Y. *Analyst*, **128**, 686 (2003).

40. West J.L., Halas N.J. *Annu. Rev. Biomed. Eng.*, **5**, 285 (2003).

41. Hirsch L.R., Gobin A.M., Lowery A.R., Tam F., Drezek R., Halas N.J., West J.L. *Annals. Biomed. Eng.*, **34**, 15 (2006).

42. Wang H., Brandl D.W., Le F., Nordlander P., Halas N.J. *Nano Lett.*, **6**, 827 (2006).

43. Nehl C.L., Liao H., Hafner J.H. *Nano Lett.*, **6**, 683 (2006).

44. Ramakrishna G., Dai Q., Zou J., Huo Q., Goodson T. III. *J. Am. Chem. Soc.*, **129**, 1848 (2007).

45. Chen J., Saeki F., Wiley B.J., Cang H., Gobb M.J., Li Zh.-Y., Au L., Zhang H., Kimmey M.B., Li X., Xia Y. *Nano Lett.*, **5**, 473 (2005); Chen J., Wiley B., Li Zh.-Y., Campbell D., Saeki F., Cang H., Au L., Lee J., Li X., Xia Y. *Adv. Mater.*, **17**, 2255 (2005).

46. Rayleigh D.W. *Phil. Mag.*, **41**, 107, 274 (1871); **44**, 28 (1897).

47. Mie G. *Ann. Phys.*, **25**, 377 (1908).

48. Gans R. *Ann. Phys.*, **37**, 881 (1912).

49. Khlebtsov B.N., Khlebtsov N.G. *J. Quant. Spectr. Radiat. Transf.*, **106**, 154 (2007).

50. Khlebtsov N.G., Mel'nikov A.G., Bogatyrev V.A., Dykman L.A., Alekseeva A.V., Trachuk L.A., Khlebtsov B.N. *J. Phys. Chem. B*, **109**, 13578 (2005).

51. Gryczynski Z., Lukomska J., Lakowicz J.R., Matveeva E.G., Gryczynski I. *Chem. Phys. Lett.*, **421**, 189 (2006); Calander N., Gryczynski I., Gryczynski Z. *Chem. Phys. Lett.*, **434**, 326 (2007).

52. Khlebtsov N.G., Trachuk L.A., Melnikov A.G. *Proc. SPIE Int. Soc. Opt. Eng.*, **5475**, 1 (2004).

53. Khlebtsov N.G., Trachuk L.A., Mel'nikov A.G. *Opt. Spekrosk.*, **97**, 105 (2004) [*Opt. Spectrosc.*, **97**, 97 (2004)].

54. Millstone J.E., Park S., Shuford K.L., Qin L., Schatz G.C., Mirkin C.A. *J. Am. Chem. Soc.*, **127**, 5312 (2005).

55. Payne E.K., Shuford K.L., Park S., Schatz G.C., Mirkin C.A. *J. Phys. Chem. B*, **110**, 2150 (2006).

56. Khlebtsov B.N., Khlebtsov N.G. *J. Phys. Chem. C*, **111**, 11516 (2007).

57. Khlebtsov B.N., Melnikov A.G., Khlebtsov N.G. *J. Quant. Spectr. Radiat. Transf.*, **107**, 306 (2007).

58. Khlebtsov N.G. *Opt. Spektrosk.*, **88**, 656 (2000) [*Opt. Spectrosc.*, **88**, 594 (2000)].

59. Khlebtsov B.N., Melnikov A.G., Zharov V.P., Khlebtsov N.G. *Nanotechnology*, **17**, 1437 (2006).

60. Wei A., in *Nanoparticles: Building Blocks for Nanotechnology* (New York: Kluwer/Plenum Publ., 2004) Ch. 5, pp 173–200.

61. Markel V.A. *J. Mod. Opt.*, **40**, 2281 (1993).

62. Tamaru H., Kuwata H., Miyazaki H.T., Miyano K. *Appl. Phys. Lett.*, **80**, 1826 (2002).

63. Su K.-H., Wei Q.-H., Zhang X., Mock J.J., Smith D.R., Schultz S. *Nano Lett.*, **3**, 1087 (2003).

64. Wei Q.-H., Su K.-H., Durant S., Zhang X. *Nano Lett.*, **4**, 1067 (2004).

65. Jain P.K., Eustis S., El-Sayed M.A. *J. Phys. Chem. B*, **110**, 18243 (2006).

66. Zou S., Janel N., Schatz G.C. *J. Chem. Phys.*, **120**, 10871 (2004); Zou S., Schatz G.C. *J. Chem. Phys.*, **121**, 12606 (2004).

67. Markel V.A. *J. Chem. Phys.*, **122**, 097101 (2005).

68. Zou S., Schatz G.C. *J. Chem. Phys.*, **122**, 097102 (2005).

69. Markel V.A. *J. Phys. B*, **38**, L115 (2005).

70. Lamprecht B., Schider G., Lechner R.T., Ditlbacher H., Krenn J.R., Leitner A., Aussenegg F.R. *Phys. Rev. Lett.*, **84**, 4721 (2000).

71. Zhao L.L., Kelly K.L., Schatz G.C. *J. Phys. Chem. B*, **107**, 7343 (2003).

72. Haynes C.L., McFarland A.D., Zhao L.L., Schatz G.C., Van Duyne R.P., Gunnarsson L., Prikulis J., Kasemo B., Käll M. *J. Phys. Chem. B*, **107**, 7337 (2003).

73. Genov D.A., Sarychev A.K., Shalaev V.M., Wei A. *Nano Lett.*, **4**, 153 (2004).

74. Bouhelier A., Bachelot R., Im J.S., Wiederrecht G.P., Lerondel G., Kostcheev S., Royer P. *J. Phys. Chem. B*, **109**, 3195 (2005).

75. Francoeur M., Venkata P.G., Mengüc M.P. *J. Quant. Spectr. Radiat. Transf.*, **106**, 44 (2007); Venkata P.G., Aslan M., Mengüc M.P., Videen G. *J. Heat Transf.*, **129**, 60 (2007).

76. Enoch S., Quidant R., Badenes G. *Opt. Express*, **12**, 3422 (2004).

77. Chang S.-H., Gray S.K., Schatz G. *Opt. Express*, **13**, 3150 (2005).

78. Park T., Mirin N., Lassiter J.B., Nehl C.L., Halas N.J., Nordlander P. *ACS Nano*, **2**, 25 (2008).

79. Podolskiy V.A., Sarychev A.K., Narimanov E.E., Shalaev V.M. *J. Opt. A*, **7**, S32 (2005).

80. Cortie M.B., Xu X., Ford M.J. *Phys. Chem. Chem. Phys.*, **8**, 3520 (2006).

81. Malynych S., Chumanov G. *J. Am. Chem. Soc.*, **125**, 2896 (2003); Malynych S., Chumanov G. *J. Opt. A*, **8**, 144 (2006).

82. Chumanov G., Sokolov K., Cotton T.M. *J. Phys. Chem.*, **100**, 5166 (1996).

83. Khlebtsov B.N., Khanadeev V.A., Khlebstov N.G. *Opt. Spektrosk.*, **104**, 333 (2008).

84. Mackowski D.W. *J. Quant. Spectr. Radiat. Transf.*, **109**, 770 (2008).

85. Khlebtsov B.N., Khanadeyev V.A., Jian Y., Mackowski D.W., Borghs G., Khlebtsov N.G. *Phys. Rev. B*, **77**, 035440 (2008).

86. Klimov V.V., Guzatov D.V. *Phys. Rev. B*, **75**, 024303 (2007); *Appl. Phys. A*, **89**, 305 (2007).

87. Klimov V.V., Guzatov D.V. *Kvantovaya Elektron.*, **37**, 209 (2007) [*Quantum Electron.*, **37**, 209 (2007)].

88. Markel V.A., Shalaev V.M., Stechel E.B., Kim W., Armstrong R.L. *Phys. Rev. B*, **53**, 2425 (1996).

89. Khebtsov N.G., Dykman L.A., Krasnov Ya.M., Mel'nikov A.G. *Kolloid. Zh.*, **62**, 844 (2000) [*Colloid J.*, **62**, 765 (2000)].

90. Lazarides A., Schatz G.C. *J. Phys. Chem. B*, **104**, 460 (2000).

91. Storhoff J.J., Lazarides A.A., Mucic R.C., Mirkin C.A., Letsinger R.L., Schatz G.C. *J. Am. Chem. Soc.*, **122**, 4640 (2000).

92. Leuvering J.H.W., Thal P.J.H.M., van der Waart M., Schuurs A.H.W.M. *J. Immunoassay*, **1**, 77 (1980).

93. Stoscheck C.M. *Meth. Enzymol.*, **182**, 50 (1990).

94. Mann S., Shenton W., Li M., Connolly S., Fitzmaurice D. *Adv. Mater.*, **12**, 147 (2000).

95. Thanh N.T.K., Rosenzweig Z. *Anal. Chem.*, **74**, 1624 (2002).

96. Dykman L.A., Bogatyrev V.A., Khlebtsov B.N., Khlebtsov N.G. *Anal. Biochem.*, **341**, 16 (2005).

97. Englebienne P., van Hoonacker A., Verhas M., Khlebtsov N.G. *Comb. Chem. High Throughput Screen.*, **6**, 777 (2003).

98. Otsuka H., Akiyama Y., Nagasaki Y., Kataoka K. *J. Am. Chem. Soc.*, **123**, 8226 (2002).

99. Mirkin C.A., Letsinger R.L., Mucic R.C., Storhoff J.J. *Nature*, **382**, 607 (1996).

100. Zharov V.P., Letfullin R.R., Galitovskaya E. *J. Phys. D: Appl. Phys.*, **38**, 2571 (2005).

101. Karpov S.V., Gerasimov V.S., Isaev I.L., Markel V.A. *Phys. Rev. B*, **72**, 205425 (2005).

102. Karpov S.V., Gerasimov S.V., Isaev I.L., Podavalova O.P., Salabko V.V. *Kolloid. Zh.*, **69**, 179 (2007).

103. Karpov S.V., Gerasimov S.V., Grachev A.S., Isaev I.L., Podavalova O.P., Salabko V.V. *Kolloid. Zh.*, **69**, 190 (2007).

104. Zhang F.X., Han Li, Israel L.B., Daras J.G., Maye M.M., Ly N.K., Zhong C.-J. *Analyst*, **127**, 462 (2002).

105. Liao J., Zhang Y., Yu W., Xu L., Ge C., Liu J., Gu N. *Colloids Surf. A*, **223**, 177 (2003).

106. Yang Y., Matsubara Sh., Nogami M., Shi J., Huang W. *Nanotechnology*, **17**, 2821 (2006).

107. Karpov S.V., Slabko V.V. *Opticheskie i fotofizicheskie svoistva fraktal'no-struktuririovannykh solei metallov (Optical and Photophysical Properties of Fractal-Structured Metal Sols)* (Novosibirsk: Siberian Branch, RAS, 2003).

108. Chang J.-Y., Wu H., Chen H., Ling Y.-C., Tan W. *Chem. Commun.*, **8**, 1092 (2005).

109. Krasnov Ya.M. *Isledovanie agregatsii nanochastits kolloidnogo zolota i ikh kon'yugatov s polimerami (Study of the Aggregation of Colloidal Gold Nanoparticles and their Conjugates with Biopolymers)*, Cand. Diss. (Saratov: Institute of Biochemistry and Physiology of Plants and Microorganisms, RAS, 2003).

110. Bohren C.F., Huffman D.R. *Absorption and Scattering of Light by Small Particles* (New York: Wiley, 1983).

111. Kelly K.L., Coronado E., Zhao L.L., Schatz G.C. *J. Phys. Chem. B*, **107**, 668 (2003).

112. Chiappetta P. *J. Phys. A: Math. Gen.*, **13**, 2101 (1980).

113. Livesay D.E., Chen K.M. *IEEE Trans. Microw. Theory Tech.*, **22**, 1273 (1974); Hage J.I., Greenberg J.M. *Astrophys. J.*, **361**, 251 (1990); Lakhtakia A. *Int. J. Mod. Phys.*, **3**, 583 (1992).

114. Landau L.D., Lifshits E.M. *The Classical Theory of Fields, 4th English ed.* (Oxford: Pergamon Press, 1975; Moscow: Fizmatgiz, 1961).

115. Draine B.T. *Astrophys. J.*, **333**, 848 (1988); Goedecke G.H., O'Brien S.G. *Appl. Opt.*, **27**, 2431 (1988).

116. Draine B.T., Goodman J. *Astrophys. J.*, **405**, 685 (1993); Gutkowicz-Krusin D., Draine B.T. http://arxiv.org/abs/astro-ph/0403082; Peltoniemi J.I. *J. Quant. Spectrosc. Radiat. Transf.*, **55**, 637 (1996).

117. Yurkin M.A. *Discrete Dipole Simulations of Light Scattering by Blood Cells* (PhD Thesis) (Amsterdam: Univ. of Amsterdam, 2007).

118. Doyle W.T. *Phys. Rev.*, **111**, 1067 (1958).

119. Doremus R.H. *J. Chem. Phys.*, **40**, 2389 (1964).

120. Römer H., von Fragstein C. *Z. Physik*, **163**, 27 (1961).

121. Doyle W.T., Agarwal A. *J. Opt. Soc. Am.*, **55**, 305 (1965).

122. Doyle W.T. *Phys. Rev. B*, **39**, 9852 (1989).

123. Kreibig U., von Fragstein C. *Z. Phys. A*, **224**, 307 (1969).

124. Kreibig U. *J. Phys. F: Met. Phys.*, **4**, 999 (1974).

125. Genzel L., Martin T.P., Kreibig U. *Z. Phys. B. Condens. Matter.*, **21**, 339 (1975).

126. Hovel H., Fritz S., Hilger A., Kreibig U., Vollmer M. *Phys. Rev. B*, **48**, 18178 (1993).

127. Granqvist C.G., Hunderi O. *Phys. Rev. B*, **16**, 3513 (1977).

128. Granqvist C.G., Buhrman R.A., Wyns J., Sievers A.J. *Phys. Rev. Lett.*, **37**, 625 (1976).

129. Granqvist C.G., Hunderi O. *Z. Phys. B*, **30**, 47 (1978).

130. Khlebtsov N.G., Bogatyrev V.A., Dykman L.A., Melnikov A.G. *J. Colloid Interface Sci.*, **180**, 436 (1996).

131. Palik E.D. (Ed.) *Handbook of Optical Constants of Solids* (New York: Acad. Press, 1985) Pt. I; 1991, Pt. II; 1998, Pt. III.

132. Coronado E.A., Schatz G.C. *J. Chem. Phys.*, **119**, 3926 (2003).

133. Quinten M. *Z. Phys. B*, **101**, 211 (1996).

134. Kreibig U. *Z. Phys.*, **234**, 307 (1970).

135. Johnson P.B., Christy R.W. *Phys. Rev. B*, **6**, 4370 (1972).

136. Scaffardi L.B., Tocho J.O. *Nanotechnology*, **17**, 1309 (2006).

137. Kachan S.M., Ponyavina A.N. *J. Mol. Struct.*, **267**, 563 (2001).

138. Khlebtsov B.N., Khlebtsov N.G. *J. Biomed. Opt.*, **11**, 44002 (2006).

139. Liu M., Guyot-Sionnest P. *J. Phys. Chem. B*, **108**, 5882 (2004).

140. Mulvaney P. *Langmuir*, **12**, 788 (1996).

141. Persson B.N.J. *Surface Sci.*, **281**, 153 (1993).

142. Halperin W.P. *Rev. Mod. Phys.*, **58**, 533 (1986).

143. Kawabata A., Kubo R. *J. Phys. Soc. Jpn*, **21**, 1765 (1966).

144. Kreibig U., Genzel L. *Surface Sci.*, **156**, 678 (1985); Zaremba E., Persson B.N.J. *Phys. Rev. B*, **35**, 596 (1987).

145. Yannouleas C., Broglia R.A. *Ann. Phys. (NY)*, **217**, 105 (1992).

146. Brack M. *Rev. Mod. Phys.*, **65**, 677 (1993).

147. Prodan E., Nordlander P. *Chem. Phys. Lett.*, **352**, 140 (2002).

148. Prodan E., Nordlander P. *Chem. Phys. Lett.*, **360**, 325 (2002).

149. Bruzzone S., Arrighini G.P., Guidotti C. *Chem. Phys.*, **291**, 125 (2003).

150. Weick G. *Quantum Dissipation and Decoherence of Collective Excitations in Metallic Nanoparticles* (PhD Thesis) (Universite Louis Pasteur, Strasbourg and Universitat Augsburg, 2006).

151. Wang H., Brandl D.W., Nordlander P., Halas N.J. *Acc. Chem. Res.*, **40**, 53 (2007).

152. Prodan E., Radloff C., Halas N.J., Nordlander P. *Science*, **302**, 419 (2003).

153. Kerker M. *J. Colloid Interface Sci.*, **105**, 297 (1985).

154. Scaffardi L.B., Pellegri N., de Sanctis O., Tocho J.O. *Nanotechnology*, **16**, 158 (2005).

155. Westcott S.L., Jackson J.B., Radloff C., Halas N.J. *Phys. Rev. B*, **66**, 155431 (2002).

156. Khlebtsov B.N., Bogatyrev V.A., Dykman L.A., Khlebtsov N.G. *Opt. Spektrosk.*, **102**, 269 (2007) [*Opt. Spectrosc.*, **102**, 233 (2007)].

157. Draine B.T., in *Light Scattering by Nonspherical Particles: Theory, Measurements, and Applications*. Ed. by M.I. Mishchenko, J.W. Hovenier, L.D. Travis (San Diego: Acad. Press, 2000) Ch.5, pp 131–145.

158. Mishchenko M.I., Travis L.D., Lacis A.A. *Scattering, Absorption, and Emission of Light by Small Particles* (Cambridge: Cambridge Univ. Press, 2002).

159. Schultz S., Smith D.R., Mock J.J., Schultz D.A. *Proc. Natl. Acad. Sci. USA*, **97**, 996 (2000).

160. Hu M., Novo C., Funston A., Wang H., Staleva H., Zou S., Mulvaney P., Xia Y., Hartland G.V. *J. Mater. Chem.*, **18**, 1949 (2008).

161. Sonnichsen C., Franzl T., Wilk T., von Plessen G., Feldmann J., Wilson O., Mulvaney P. *Phys. Rev. Lett.*, **88**, 077402 (2002).

162. Novo C., Gomez D., Perez-Juste J., Zhang Z., Petrova H., Reismann M., Mulvaney P., Hartland G.V. *Phys. Chem. Chem. Phys.*, **8**, 3540 (2006).

163. Hu M., Marquez M., Xia Y., Hartland G.V. *J. Phys. Chem. C*, **111**, 12558 (2007).

164. Wokaun A., Gordon J.P., Liao P.F. *Phys. Rev. Lett.*, **48**, 957 (1982).

165. Berciaud S., Cognet L., Tamarat P., Lounis B. *Nano Lett.*, **5**, 515 (2005).

166. Scharte M., Porath R., Ohms T., Aeschlimann M., Krenn J.R., Ditlbacher H., Aussenegg F.R., Liebsch A. *Appl. Phys. B*, **73**, 305 (2001).

167. Nehl C.L., Grady N.K., Goodrich G.P., Tam F., Halas N.J., Hafner J.H. *Nano Lett.*, **4**, 2355 (2004).

168. Arbouet A., Christofilos D., Del Fatti N., Vallee F., Huntzinger J.R., Arnaud L., Billaud P., Broyer M. *Phys. Rev. Lett.*, **93**, 127401 (2004).

169. Lindfors K., Kalkbrenner T., Stoller P., Sandoghdar V. *Phys. Rev. Lett.*, **93**, 037401 (2004).

170. Ignatovich F.V., Novotny L. *Phys. Rev. Lett.*, **96**, 013901 (2006).

171. Stoller P., Jacobsen V., Sandoghdar V. *Opt. Lett.*, **13**, 2474 (2006).

172. Berciaud S., Cognet L., Tamarat P., Lounis B. *Nano Lett.*, **5**, 515 (2005).

173. Muskens O.L., Del Fatti N., Vallee F., Huntzinger J.R., Billaud P., Broyer M. *Appl. Phys. Lett.*, **88**, 0634109 (2006).

174. Schulz L.G. *J. Opt. Soc. Am.*, **44**, 357 (1954); Schulz L.G., Tangherlini F.R. *J. Opt. Soc. Am.*, **44**, 362 (1954).

175. Irani G.B., Huen T., Wooten F. *J. Opt. Soc. Am.*, **61**, 128 (1971).

176. Otter M. *Z. Physik*, **161**, 163 (1961).

177. Hagemann H.-J., Gudat W., Kunz C. *Optical Constants from the Far Infrared to the X-ray Region: Mg, Al, Cu, Ag, Bi, C, and Al$_2$O$_3$* (Hamburg: Deutsches electronen-synchrotron DESY SR-74/7, 1974).

178. Canifeld L.R., Hass G., Hunter W.R. *J. Phys. (Paris)*, **25**, 124 (1964).

179. Taflove A., Hagness S.C. *Advances in Computational Electrodynamics: The Finite-Difference Time-Domain Method* (Boston: Artech House, 2005).

180. Oubre Ch., Nordlander P. *J. Phys. Chem. B*, **108**, 17740 (2004).

181. Underwood S., Mulvaney P. *Langmuir*, **10**, 3427 (1994).

182. Faraday M. *Phil. Trans. Royal. Soc.* (Ldn), **147**, 145 (1857).

183. Zsigmondy R. *Ann. Chim.*, **301**, 29 (1898).

184. Svedberg T. *Colloid Chemistry* (New York: Chemical Catalog Co., 1928).

185. Yguerabide J., Yguerabide E. *J. Cell. Biochem. Suppl.*, **37**, 71 (2001).

186. Bogatyrev V.A., Dykman L.A., Krasnov Ya.M., Plotnikov V.K., Khlebtsov N.G. *Kolloid. Zh.*, **64**, 745 (2002) [*Colloid J.*, **64**, 671 (2002)].

187. Bogatyrev V.A., Dykman L.A., Khlebtsov B.N., Khlebtsov N.G. *Opt. Spektrosk.*, **96**, 139 (2004) [*Opt. Spectrosc.*, **96**, 128 (2004)].

188. Khlebtsov N.G., Bogatyrev V.A., Dykman L.A., Khlebtsov B.N., Krasnov Ya.M. *J. Quant. Spectrosc. Radiat. Transf.*, **89**, 133 (2004).

189. Frens G. *Nature Phys. Sci.*, **241**, 20 (1973).

190. Nowicki W. *Colloids Surf. A*, **194**, 159 (2001).

191. Doron A., Joselevich E., Schlittner A., Willner I. *Thin Solid Films.*, **340**, 183 (1999).

192. Brown K.R., Walter D.G., Natan M.J. *Chem. Mater.*, **12**, 306 (2000).

193. Brown K.R., Natan M.J. *Langmuir*, **14**, 726 (1998).

194. Chithrani B.D., Ghazani A.A., Chan W.C.W. *Nano Lett.*, **6**, 662 (2006).

195. Andreescu D., Sau T.K., Goia D.V. *J. Colloid Interface Sci.*, **298**, 742 (2006).

196. Horisberger M., in *Techniques in Immunocytochemistry*. Ed. by G.R. Bullock, P. Petrusz (London: Acad. Press, 1985) p. 155.

197. Slouf M., Kuzel R., Matej Z. *Z. Kristallogr. Suppl.*, **23**, 319 (2006).

198. Njoki P.N., Lim I.-I.S., Mott D., Park H.-Y., Khan B., Mishra S., Sujakumar R., Luo J., Zhong C.-J. *J. Phys. Chem. B*, **111**, 14664 (2007).

199. Haiss W., Thanh N.T.K., Aveard J., Fernig D.G. *Anal. Chem.*, **79**, 4215 (2007).

200. Ung T., Liz-Marzán L.M., Mulvaney P. *J. Phys. Chem. B*, **105**, 3441 (2001).

201. Link S., Mohamed M.B., El-Sayed M.A. *J. Phys. Chem. B*, **103**, 3073 (1999).

202. Sosa I.O., Noguez C., Barrera R.G. *J. Phys. Chem. B*, **107**, 6269 (2003).

203. Alekseeva A.V., Bogatyrev V.A., Dykman L.A., Khlebtsov B.N., Trachuk L.A., Melnikov A.G., Khlebtsov N.G. *Appl. Opt.*, **44**, 6285 (2005).

204. Brioude A., Jiang X.C., Pileni M.P. *J. Phys. Chem. B*, **109**, 13138 (2005).

205. Jiang X.C., Brioude A., Pileni M.P. *Colloids Surf. A*, **277**, 201 (2006).

206. Xu X., Cortie M.B. *Adv. Funct. Mater.*, **6**, 2170 (2006).

207. Prescott W., Mulvaney P. *J. Appl. Phys.*, **99**, 123504 (2006).

208. Kooij E.S., Poelsma B. *Phys. Chem. Chem. Phys.*, **6**, 3349 (2006).

209. Khlebtsov N.G., Mel'nikov A.G., Bogatyrev V.A., Alekseeva A.V., Khlebtsov B.N. *Opt. Spektrosk.*, **100**, 495 (2006) [*Opt. Spectrosc.*, **100**, 448 (2006)].

210. Aaron J., de la Rosa E., Travis K., Harrison N., Burt J., José-Yakamán M., Sokolov K. *Opt. Express*, **16**, 2153 (2008).

211. Van de Hulst H.C. *Light Scattering by Small Particles* (NewYork: Wiley, 1957).

212. Kerker M. *The Scattering of Light and Other Electromagnetic Radiation* (New York: Academic, 1969).

213. Berestetskii V.B., Lifshits E.M., Pitaevskii L.P. *Relativistic Quantum Theory* (Oxford: Pergamon Press, 1971; Moscow: Fizmatlit, 2006).

214. Al-Sherbini A.-S.A.-M. *Colloids Surf. A*, **246**, 61 (2004).

215. Orendorff Ch.J., Murphy C.J. *J. Phys. Chem. B*, **110**, 3990 (2006).

216. Sonnichsen C., Alivisatos A.P. *Nano Lett.*, **5**, 301 (2005).

217. Bogatyrev V.A., Dykman L.A., Alekseeva A.V., Khlebtsov B.N., Novikova A.P., Khlebtsov N.G. *Proc. SPIE Int. Soc. Opt. Eng.*, **6164**, 616401 (2006).

218. Orendorff C.J., Sau T.K., Murphy C.J. *Small*, **2**, 636 (2006).

219. Oldenburg A.L., Hansen M.N., Zweifel D.A., Wei A., Boppart S.A. *Opt. Express*, **14**, 6724 (2006).

220. Kalele S., Gosavi S.W., Urban J., Kulkarni S.K. *Current Sci.*, **91**, 1038 (2006).

221. Hirsch L.R., Jackson J.B., Lee A., Halas N.J., West J.L. *Anal. Chem.*, **75**, 2377 (2003).

222. Khlebtsov B.N., Dykman L.A., Bogatyrev V.A., Zharov V.P., Khlebtsov N.G. *Nanoscale Res. Lett.*, **2**, 6 (2007).

223. Huang X., Jain P.K., El-Sayed M.A. *Lasers in Medical Science*, Aug. 3, DOI 10.1007/s10103-007-0470-x (2007).

224. Bernardi R.J., Lowery A.R., Thompson P.A., Blaney S.M., West J.L. *J. Neurooncol*, **86**, 165 (2008).

225. Akchurin G., Khlebtsov B., Akchurin G., Tuchin V., Zharov V., Khlebtsov N. *Nanotechnology*, **19**, 015701 (2008).

226. Pham T., Jackson J.B., Halas N., Lee T.R. *Langmuir*, **18**, 4915 (2002).

227. Pellegrino T., Kudera S., Liedl T., Javier A.M., Manna L., Parak W.J. *Small*, **1**, 48 (2005).

228. Khlebtsov N.G., Dykman L.A., Bogatyrev V.A., Khlebtsov B.N. *Kolloid. Zh.*, **65**, 552 (2003) [*Colloid J.*, **65**, 508 (2003)].

229. Khlebtsov N.G., Dykman L.A., Bogatyrev V.A., Khlebtsov B.N., Englebienne P. *Kolloid. Zh.*, **65**, 679 (2003) [*Colloid J.*, **65**, 622 (2003)].

230. Khlebtsov N.G. *J. Quant. Spectrosc. Radiat. Transf.*, **89**, 143 (2004).

231. Khlebtsov B.N., Khlebtsov N.G. *Proc. SPIE Int. Soc. Opt. Eng.*, **6164**, 616405 (2006).

232. Trachuk L.A., Vrublevsky S.A., Khlebtsov B.N., Melnikov A.G., Khlebtsov N.G. *Proc. SPIE Int. Soc. Opt. Eng.*, **5772**, 1 (2005); Trachuk L.A., Melnikov A.G., Khlebtsov B.N., Khlebtsov N.G. *Proc. SPIE Int. Soc. Opt. Eng.*, **5829**, 127 (2005).

233. Trachuk L.A. *Opticheskie svoistva nanochastits zolota i serebra v svazi s zadachami biodiagnostiki* (Optical Properties of Gold and Silver Particles Related to the Problems of Biodiagnostics), Cand. Diss. (Saratov: Institute of Biochemistry and Physiology of Plants and Microorganisms, RAS, 2007).

234. Khlebtsov N.G., Trachuk L.A., Mel'nikov A.G. *Opt. Spektrosk.*, **98**, 83 (2005) [*Opt. Spectrosc.*, **98**, 77 (2005)].

235. Chen K., Liu Y., Ameer G., Backman V. *J. Biomed. Opt.*, **10**, 024005 (2005).

236. Khlebtsov B.N., Khlebtsov N.G. *Proc. SPIE Int. Soc. Opt. Eng.*, **6164**, 616402 (2006).

237. Miller M.M., Lazarides A.A. *Phys. Chem. B*, **109**, 21556 (2005).

238. Xu H., Kall M. *Sens. Actuators B*, **87**, 244 (2002).

239. Nath N., Chilkoti A. *Anal. Chem.*, **76**, 5370 (2004).

240. Barber P.W., Chang R.K., Massoudi H. *Phys. Rev. B*, **27**, 7251 (1983).

241. Jin R., Cao Y.W., Mirkin C.A., Kelly K.L., Schatz G.C., Zheng J.G. *Science*, **294**, 1901 (2001).

242. Krenn J.R., Schider G., Rechberger W., Lamprecht B., Leitner A., Aussenegg F.R., Weeber J.C. *Appl. Phys. Lett.*, **77**, 3379 (2000).

243. Laurent G., Felidj N., Aubard J., Levi G., Krenn J.R., Hohenau A., Schider G., Leitner A., Aussenegg F.R. *J. Chem. Phys.*, **122**, 011102 (2005).

244. Schider G., Krenn J.R., Hohenau A., Ditlbacher H., Leitner A., Aussenegg F.R., Schaich W.L., Puscasu I., Monacelli B., Boreman G. *Phys. Rev. B*, **68**, 155427 (2003).

245. Schaich W.L., Schider G., Krenn J.R., Leitner A., Aussenegg F.R., Puscasu I., Monacelli B., Boreman G. *Appl. Opt.*, **42**, 5714 (2003).

246. Lim J.K., Imura K., Nagahara T., Kim S.K., Okamoto H. *Chem. Phys. Lett.* **412**, 41 (2005).

247. Okamoto H., Imura K. *J. Mater. Chem.*, **16**, 3920 (2006).

248. Khlebtsov N.G. *Appl. Opt.*, **31**, 5359 (1992).

249. Calander N. *Curr. Anal. Chem.*, **2**, 203 (2006).

250. Dykman L.A., Krasnov Ya.M., Bogatyrev V.A., Khlebtsov N.G. *Proc. SPIE Int. Soc. Opt. Eng.*, **4241**, 37 (2001).

251. Baptista P.V., Koziol-Montewka M., Paluch-Oles J., Doria G., Franco R. *Clinical Chemistry*, **52**, 1433 (2006).
252. Doria G., Franco R., Baptista P. *IET Nanobiotechnol.*, **1**, 53 (2007).
253. Liu X., Dai Q., Austin L., Coutts J., Knowles G., Zou J., Chen H., Huo Q. *J. Am. Chem. Soc.*, DOI: 10.1021/ja711298b (2008).
254. Butler J.E. (Ed.) *Immunochemistry of Solid-Phase Immunoassay* (Boca Raton: CRC Press Inc., 1991).
255. Hawkes R., Niday E., Gordon J. *Anal. Biochem.*, **119**, 142 (1982).
256. Santos N.C., Castanho M.A.R.B. *Biophys. Chem.*, **107**, 133 (2004).
257. Evtushenko E.G., Kurochkin I.N., Dontsova E.A., Budashov I.A., Eremenko A.V., Golovachenko V.A., Pllyntsev D.G., Tur D.R., Pergushov D.V., Pakov I.S., Zezin A.B., Varfolomeev S.D. *Ross. Nanotekhnol.*, **2**, 145 (2007).
258. Blab G.A., Cognet L., Berciaud S., Alexandre I., Husar D., Remacle J., Lounis B. *Biophys. J.*, **90**, L13 (2006).
259. Raschke G., Kowarik S., Franzl T., Sonnichsen C., Klar T.A., Feldmann J., Nichtl A., Kurzinger K. *Nano Lett.*, **3**, 935 (2003); McFarland A.D., Van Duyne R.P. *Nano Lett.*, **3**, 1057 (2003).
260. Starodub N.F., Artyukh V.P., Nazarenko V.I., Kolomiets L.I. *Ukr. Biokhim. Zh.*, **59**, 108 (1987).
261. Furuya T., Ikemoto K., Kawauchi S., Oga A., Tsunoda S., Hirano T., Sasaki K. *J. Histochem. Cytochem.*, **52**, 205 (2004).
262. Duan L., Wang Y., Li Sh.Sh.-ch., Wan Zh., Zhai J. *BMC Infectious Diseases*, **5**, 53 (2005).
263. Han A., Dufva M., Belleville E., Christensen C.B.V. *Lab. Chip*, **3**, 329 (2003).
264. Prokopenko D.V., Chechetkin V.R., Makarov A.A., Zasedatelev A.S. *Ross. Nanotekhnol.*, **1**, 13 (2006).
265. Vaessen R.T.M.J., Kreike J., Groot G.S.P. *FEBS Lett.*, **124**, 193 (1981).
266. Brada D., Roth J. *Anal. Biochem.*, **142**, 79 (1984); Moeremans M., Daneles G., van Dijck A., Langanger G., De Mey J. *J. Immunol. Meth.*, **74**, 353 (1984); Surek B., Latzko E. *Biochem. Biophys. Res. Commun.*, **121**, 284 (1984); Hsu Y.-H. *Anal. Biochem.*, **142**, 221 (1984).
267. Gupta Sh., Huda S., Kilpatrick P.K., Velev O.D. *Anal. Chem.*, **79**, 3810 (2007).
268. Liang R.Q., Tan C.Y., Ruan R.C. *J. Immunol. Meth.*, **285**, 157 (2004).
269. Hou S.-Y., Chen H.-K., Cheng H.-C., Huang C.-Y. *Anal. Chem.*, **79**, 980 (2007).
270. Cao C., Sim S.J. *Biosens. Bioelectron.*, **22**, 1874 (2007); Han S.-M., Cho J.-H., Cho I.-H., Paek E.-H., Oh H.-B., Kim B.-S., Ryu Ch., Lee K., Kim Y.-K., Paek S.-H. *Anal. Chim. Acta.*, **587**, 1 (2007).
271. Koo H.C., Park Y.H., Ahn J., Waters W.R., Palmer M.V., Hamilton M.J., Barrington G., Mosaad A.A., Park K.T., Jung W.K.H., In Y., Cho S.-N., Shin S.J., Davis W.C. *J. Clin. Microbiol.*, **43**, 4498 (2005).
272. Peng Z., Chen Z., Jiang J., Zhang X., Shen G., Yu R. *Anal. Chim. Acta*, **583**, 40 (2007).
273. Zhang S.-B., Wu Z.-S., Guo M.-M., Shen G.-L., Yu R.-Q. *Talanta*, **71**, 1530 (2007).
274. Zhang H., Meyerhoff M.E. *Anal. Chem.*, **78**, 609 (2006).
275. Khlebtsov B.N., Khanadeev V.A., Bogatyrev V.A., Dykman L.A., Khlebtsov N.G. *Nanotechnologies in Russia*, **3**, 442 (2008).
276. Aaron J., Nitin N., Travis K., Kumar S., Collier T., Park S.Y., Jose-Yacaman M., Coghlan L., Follen M., Richards-Kortum R., Sokolov K. *J. Biomed. Opt.*, **12**, 034007 (2007).
277. Bao P., Frutos A.G., Greef Ch., Lahiri J., Muller U., Peterson T.C., Warden L., Xie X. *Anal. Chem.*, **74**, 1792 (2002).
278. Imura K., Nagahara T., Okamoto H. *J. Phys. Chem. B*, **109**, 13214 (2005).
279. Huff T.B., Hansen M.N., Zhao Y., Cheng J.-X., Wei A. *Langmuir*, **23**, 1596 (2007).
280. Durr N.J., Larson T., Smith D.K., Korgel B.A., Sokolov K., Ben-Yakar A. *Nano Lett.*, **7**, 941 (2007).
281. Park J., Estrada A., Sharp K., Sang K., Schwartz J.A., Smith D.K., Coleman Ch., Payne J.D., Korgel B.A., Dunn A.K., Tunnell J.W. *Opt. Express*, **16**, 1590 (2008).
282. Sokolov K., Follen M., Aaron J., Pavlova I., Malpica A., Lotan R., Richards-Kortum R. *Cancer Res.*, **63**, 1999 (2003).
283. Zharov V., Galanzha E., Shashkov E., Khlebtsov N., Tuchin V. *Opt. Lett.*, **31**, 3623 (2006).
284. Mallidi S., Larson T., Aaron J., Sokolov K., Emelianov S. *Opt. Express*, **15**, 6583 (2007).
285. Larson T.A., Bankson J., Aaron J., Sokolov K. *Nanotechnology*, **18**, 325101 (2007).
286. Chithrani B.D., Chan W.C.W. *Nano Lett.*, **7**, 1542 (2007); Giljohann D.A., Seferos D.S., Patel P.C., Millstone J.E., Rosi N.L., Mirkin C.A. *Nano. Lett.*, **7**, 3818 (2007); Jiang W., Kim B.Y.S., Rutka J.T., Chan W.C.W. *Nature Nanotechnology*, **3**, 145 (2008).
287. De Jong W.H., Hagens W.I., Krystek P., Burger M.C., Sips A.J.A.M., Geertsma R.E. *Biomaterials*, **29**, 1912 (2008).
288. Park S.Y., Lytton-Jean A.K., Lee B., Weigand S., Schatz G.C., Mirkin Ch.A. *Nature*, **451**, 553 (2008).
289. Nykypanchuk D., Maye M.M., van der Lelie D., Gang O. *Nature*, **451**, 549 (2008).